國 立 交 通 大 學

機械工程學系

碩 士 論 文

運用狀態觀察器技術之車輛翻覆預測系統

Vehicle Rollover Prediction System
Using States Observers

研 究 生：許齡元

指導教授：陳宗麟　博士

中 華 民 國 九 十 五 年 七 月

運用狀態觀察器技術之車輛翻覆預測系統

Vehicle Rollover Prediction System Using States Observers

研 究 生：許齡元　　Student：Ling-Yuan Hsu

指導教授：陳宗麟　　Advisor：Tsung-Lin Chen

國 立 交 通 大 學

機 械 工 程 學 系

碩 士 論 文

A Thesis
Submitted to Department of Mechanical Engineering
College of Engineering
National Chiao Tung University
in Partial Fulfillment of the Requirements
for the Degree of
Master of Science

in

Mechanical Engineering

July 2006

Hsinchu, Taiwan, Republic of China

中華民國九十五年七月

運用狀態觀察器技術之車輛翻覆預測系統

學生: 許齡元　　指導教授: 陳宗麟 博士

國立交通大學機械工程學系 碩士班

摘　要

在本篇論文中，我們提出了一個車輛翻覆預測系統。此一系統主要是以含有道路狀況之”完整車輛模型”為出發點，藉由狀態觀察器技術來獲得車輛即時動態，並且將即時動態傳輸至車輛模型中，來預測在未來時間內的車輛動態，進而以在未來時間內的車輛側傾角，判斷車輛是否即將翻覆。此種預測方法能應用於各種不同動態的車型，並提供可靠的物理根據來宣告車輛翻覆事件。

此預測系統的挑戰之一為如何建立以完整車輛模型（高階、高度非線性系統）為基礎之狀態觀察器。我們提出一適用於非線性系統之新型觀察矩陣，藉由此觀察矩陣來簡化完整車輛模型，並拆解成兩個低階子模型：側傾、橫擺子模型。如此一來，即可針對兩低階子模型分別建立狀態觀察器，再經由相似於傳統 ADI(Alternative Direction Implicit)之切換式數值演算法，來進行車輛即時動態估測。由本論文中的 ADI-like 切換式演算機制之收斂穩定度分析中可知，此演算機制能成功的使兩個從複雜系統中解析出之子系統，近似於原複雜系統之動態行為。

由模擬結果得知，當車輛在一斜坡上做快速轉彎之操作行為下，上述之觀察器演算機制可藉由三種感測器：縱向速度感測器、側向加速度感測器以及懸掛系統位移感測器，來正確地預測出車輛翻覆之發生。

Vehicle Rollover Prediction System Using States Observers

Student: Ling-Yuan Hsu Advisor: Dr. Tsung-Lin Chen

Department of Mechanical Engineering

National Chiao-Tung University

Abstract

In this thesis, we present a vehicle rollover prediction method, which employs the "full-car model" accompanied with road conditions and states observer techniques, to predict vehicle dynamics and declare a rollover happening by the vehicle roll angle in future time. This prediction method presents a strong evidence for a rollover occurrence, and the methodology can be widely applied to vehicles with different dynamic characteristics.

Based on the novel observability matrix proposed in this thesis, the "full-car model" is broken down into two subsystems. Two states observers are constructed for each subsystem respectively and do the switching scheme for the vehicle states estimation, which the approach is similar to the conventional alternative direction implicit method (ADI). The proposed ADI-like computation scheme enables a states observer design for a highly nonlinear and high order dynamic system.

Simulation results indicate that, with the following three sensors: longitudinal velocity sensor, lateral accelerometer and suspension displacement sensor, we are able to predict a vehicle rollover occurrence correctly, which is initiated by a quick wheels maneuvering on a slope.

Acknowledgement

本論文得以完成，首先要感謝作者的指導教授陳宗麟老師，在老師的研究領導之下，能夠周詳地考量本論文中各項難題，並且指引出最佳方向，讓作者能夠輕鬆地面對挑戰。在此過程中，不但學習到相關專業知識以及技術上的應用，更學習到如何去面對各種議題，更甚於在技術中找出議題並解決。此兩年的光陰，作者在老師身上學到很多，最後，在此致上最誠摯的謝意。

同時感謝實驗室學長、同儕與學弟在各項課題的指導、在心靈層面的關懷以及在日常生活的解悶，並且在課業與研究上皆能互相砥礪求進步，使得作者能夠順利成就本論文。

順便感謝大學同窗好友，在網路上不時地給予鼓勵，能夠在充滿研究氣息的日常生活中，增加另一份趣味。

最後僅將本論文獻給最親愛的父親許添富與母親吳沂瀛，感謝他們多年來所付出的辛勞，從小以開明方式教導作者讀書，今時今日，作者才能成就此論文，希望能與他們分享成就之快樂；女友雲理，亦在本論文之過程中，能給予相當多的支持，感謝她時常舟車勞頓，並且時常鼓勵作者學習，使作者能無憂無慮之下完成此論文，在此獻上最誠摯之謝意。

Contents

List of Tables

List of Figures

Mathematical Notations

Variable symbol

E^G	:	global frame
E^W	:	wheel frame
E^B	:	body frame
E^{road}	:	road frame
Q	:	rotation orthogonal tensor for Euler transformation
$\varepsilon, \phi, \theta$	:	Euler angles presented in body frame, for yaw, roll, and pitch motion
$\varepsilon_{road}, \phi_{road}, \theta_{road}$	:	Euler angle presented in road frame, for yaw, roll, and pitch motion
ε_r	:	relative yaw angle between vehicle yaw angle and road yaw angle
x, y, z	:	vehicle displacement in longitudinal, lateral, and vertical directions
$\omega_{\phi,\theta,\varepsilon}$	:	Euler angular velocity along three Euler axes
$\omega_{x,y,z}$	:	vehicle angular velocity presented in body frame
ω_i	:	tire angular velocity in wheel frame, for i = 1~4.
L	:	angular momentum about the CG of the vehicle body
M	:	external moment about the CG of the vehicle body
σ_i	:	momentum arms associated with the ith external force
$F_{x,y,z}^{body}$	:	effective forces presented in the body frame in three directions
$F_{x,y,z}$	:	effective forces presented in the wheel frame in three directions
$F_{x,y,z}^{road}$	:	effective forces induced by road conditions and presented in road frame in three directions
Z_i^W	:	length variation at the ith suspension in wheel frame
H_i	:	spring compression of the ith suspension in wheel frame

r_{ei}	:	effective rolling radius of the *i*th tire
ρ	:	road curvature
δ_i	:	tire steering angle of the *i*th tire
λ_i	:	slip ratio of the *i*th tire
α_i	:	slip angle of the *i*th tire

Vehicle parameter symbol

$m_{vehicle}$	:	total vehicle mass from sprung mass and unsprung mass
m_s	:	sprung mass of the vehicle body
m_{ui}	:	unsprung mass of the vehicle at the *i*th side
$I_{x,y,z}$	:	moment of inertia of the vehicle along three axes
$sb_{1,2}$	:	tread width of the vehicle at the front/rear side
$l_{1,2}$	:	distance from the vehicle CG to the front/rear axle
h	:	height of the vehicle CG
Z	:	distance from the vehicle CG to the road surface
K	:	spring stiffness coefficient
C_m	:	nonlinear spring stiffness modeling, for m = 1, 2, 3
D_{damper}	:	damper coefficient
$T_{brake,i}$	:	braking torque acting on the *i*th tire
$T_{motor,i}$	:	motor torque acting on the *i*th tire
g	:	gravitational constant

Tire parameter symbol

r_i	:	real radius of the *i*th tire
I_{wheel}	:	moment of inertia of the tire along three directions
$K_{vertical}$	:	tire vertical stiffness coefficient
κ_i	:	roll steer coefficient of the *i*th tire
B, C, D, E	:	characteristic coefficients of the nonlinear tire model
γ	:	camber thrust stiffness coefficient

Chapter 1
Introduction

A vehicle rollover prediction system proposed in this thesis is to study this topic of the vehicle safety problem. This system can help drivers know where, when and how the vehicle rollover happens, and provide the dynamic information to rebuild the happened rollover accident. Furthermore, motivations and objective will be introduced in section 1.1. Section 1.2 surveys previous researches about issues extended from this prediction system. Then, the construction and organization of this thesis will be described in section 1.3 and 1.4, respectively.

1.1 Motivations and Objectives

In 1999, National Highway Traffic Safety Administration (NHTSA) announced its plan to take rollover stability in the one-to-five star rating system for safety performance. One major driving force behind this initiative was the well-published rollover incidents of several Sport Utility Vehicles and consumer passenger cars. In particular, from CBS news, 62% of all SUV deaths occurred in rollover accidents. It seems fair to say that the rollover stability has become an important measure in the car safety performance.

With the increasing amount of the car, the rise of this vehicle safety problem comes as expected. The vehicle safety performance, such as the above-mentioned star rating system, safety factor, etc., becomes one of the important factors when consumers purchase a car. However, the cost of this vehicle, equipping more safety systems, will deter consumers from buying this vehicle. Therefore, a safety system with low cost and high accuracy is necessary to be planned.

Most of the research works, which study in rollover accidents, were focus on vehicles with higher center of the gravity (CG), such as trucks, trailer, etc. [1] [18] [21] [26]. However, the dynamic maneuver of these heavy vehicles is more different than that of consumer passenger cars, even the SUV. The factor of that is heavy vehicles carry more than four tires

and in some cases, a trailer. Therefore, a proper vehicle rollover prediction system with low cost and high accuracy for four-wheel vehicles is proposed in this thesis.

1.2 Previous Research Survey

In this section, several topics studied in this thesis will be reviewed. Additionally, the topics include: dynamic modeling of full-state vehicle, prediction method in vehicle rollover, neglect of the vehicle pitch motion, and numerical algorithm in switching scheme.

1.2.1 Dynamic Modeling of Full-State Vehicle

The complication of the vehicle model is decided from concerned vehicle states. Most of previous researches were developed their own vehicle models with less degree of freedom (DOF) [4] [7] [10] [23] [27]. In order to keep accurate dynamics of the vehicle, vehicle states, which are not integrated into the vehicle model, will be supplied by empirical parameters. Furthermore, the empirical parameter, verified by the experimental data, may be only valid in some operating regions. However, this method is not suitable for rollover accidents, for the reason that the vehicle rollover may happen in any possible situation.

In contrary, some research works construct a vehicle model with complex dynamics, as shown in VDANL (Vehicle Dynamics Analysis, Non Linear) [2], CarSim [29], EDVSM (Engineering Dynamics Vehicle Simulation Model) [6], ADAMS (Agencywide Documents Access and Management System) [22], etc. With substituting vehicle geometry parameters of this vehicle model, we can obtain accurate dynamics of this vehicle in any possible operating region. However, these vehicle models hiding in the unavailable codes are not suitable for observer and/or controller design.

1.2.2 Prediction Method in Vehicle Rollover

Obviously, a credible vehicle rollover prediction method can effectively lower the amount of rollover accidents. As a result, researchers proposed various prediction methods including: time-to-rollover (TTR), rollover velocity, genetic algorithm predictor (GAP), rollover index

(RI), rollover stability advisor (RSA) and etc. [4] [10] [18] [23] [27] [28] [31]. Most of these methods employ vehicle current states information along with either heuristic formulas or over-simplified vehicle models to predict rollover happenings. These approaches may be applicable to certain rollover events and specific types of vehicles. However, they generally can not be applied to different types of vehicles nor account for different types of rollover events. This is because the vehicle rollover is a consequence of multiple vehicle dynamics, vehicle maneuvering, road conditions, etc. All these factors have to be examined carefully for an accurate vehicle rollover prediction.

1.2.3 Neglect of the Vehicle Pitch Motion

Most of the research work developed their rollover stability measure based on a simplified vehicle model. Furthermore, the frequently neglected vehicle dynamics is the pitch motion [4] [10] [19] [23] [28]. The negligence of pitch motion, or any other dynamics, in the rollover stability could be practical but it needs a feasibility check. Unfortunately, we did not find much theoretical discussion from the published materials. From the dynamic viewpoint, the system observability matrix can elucidate the connections between system output and system states [5]. This technique has been successfully utilized in determining the best sensor locations [11] [24], model reduction [5], etc. Therefore, conceptually, it is possible to adopt this technique in a rollover prediction system to examine the feasibility of a simplified vehicle model and determine the suitable sensors deployment. However, challenges arise for the case that a system of interest is highly nonlinear and involves many states. In that case, the construction of observability matrix would involve intensive math derivations and thus impractical.

1.2.4 Numerical Algorithm in Switching Scheme

Alternative Direction Implicit (ADI) [14] methods have been widely utilized in numerical calculations for partial differential equations. This method breaks a partial differential equation into a set of difference equations and doing the switching scheme mainly to save for the computation time. In this thesis, an ADI-like computation scheme is proposed to break a set of highly nonlinear differential equations into two sets of nonlinear differential equations,

not for the computation time but for obtaining less complicated subsystems. It is because most of control methodologies require vast math derivation and, in practice, can only apply to systems with less complicated math models. Similar to the ADI method, the proposed method gain its advantages at the price of simulation accuracy. Therefore, the stability and accuracy of this ADI-like method need to be resolved before use.

1.3 Construction of this Vehicle Rollover Prediction System

Theoretically, the response of a dynamic system can be well described by a precise system model and associated initial conditions. Stem from this concept, we proposed a novel vehicle rollover prediction system, which composed of an observer-based estimator and a model-based predictor. The estimator uses three sensors (longitudinal velocity sensor, lateral acceleration sensor and suspension displacement sensor) to work with a simplified vehicle model for the observer construction. The predictor uses the vehicle dynamic model along with those estimated vehicle states to predict the vehicle roll angle in future time. The predicted vehicle roll angle can be utilized to declare vehicle rollover in future time and/or determining which rollover prevention measure to implement. Furthermore, the simplified model is excerpted from the vehicle full-car model with the feasibility check via system observability matrix, and it incorporates the road bank condition. This approach, based on the well-defined system model, present a strong evidence for the vehicle rollover prediction.

1.4 Outline of this Thesis

The organization of the thesis is shown as follows.

In chapter 2, the nonlinear full-car model is presented. The sprung mass system and unsprung mass system of the vehicle are discussed and linked together. Furthermore, the road condition is also considered to be integrated into the vehicle modeling.

In chapter 3, the basic concept and procedure of the novel observability matrix along a trajectory are both presented. Then, simulation results provide the evidence for the neglect of

the vehicle pitch motion. After neglecting the vehicle pitch motion, the integrated yaw-roll model is excerpted from the full-car model.

In chapter 4, the vehicle rollover prediction system is described in detail. The components of this prediction system, such as the predictor, estimator, switching scheme, and nonlinear observer, are also introduced, respectively. Additionally, the stability analysis of the switching scheme is proved in the mathematical methodology.

In chapter 5, simulation results are shown to verify this prediction system.

In chapter 6, we summarize conclusions addressed in this thesis and the suggestions of future works.

Chapter 2

Full-Car Model

A full-car model with 21 states is constructed to mimic a moving vehicle on real road conditions. This model contains two parts: a vehicle body (sprung mass) and four wheel-axle assemblies (unsprung mass). In this thesis, the sprung-mass system assumes rigid body motion and its math derivation work mostly follows Hingwe's dissertation [13]. The unsprung-mass system contains five sub-systems, which are wheel steering system, suspension system, nonlinear tire model, wheel dynamics and road bank conditions. The mathematic models of these subsystems, which often derived for different coordinates system (dynamic frame) at its own convenience, can be integrated into one system via physical principles and Euler angle transformation.

Section 2.1 introduces some dynamic frames of the vehicle system. The sprung mass system and the unsprung mass system of the vehicle are individually introduced in the section 2.2 and 2.3. The road conditions are also considered in the vehicle modeling and described in the section 2.4. The whole dynamics equations of the vehicle model, as discussed above, are summarized in section 2.5, and then, section 2.6 will introduce how to check out the model validation. Section 2.7 describes the conclusion of the vehicle modeling.

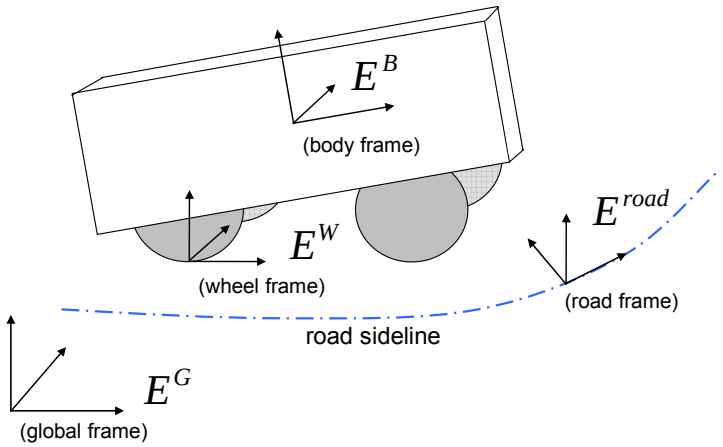

Figure 2.1 Diagram of frames about vehicle

2.1 Dynamic Frames of the Vehicle

Dynamic frames of a vehicle system, most moving objects as well, are often considered for two frames: global frame and body frame. However, these two frame systems are not convenient enough to describe the dynamics of a vehicle system, since a vehicle system can contain lots of subsystems. Therefore, we introduce 4 coordinate systems along with the vehicle dynamics modeling work. They are global frame (E^G), which is fixed to earth; road frame (E^{road}), which is set on the road and changed with the road bank angle; wheel frame (E^W), which is set on the tire; body frame (E^B), which is set on the center of gravity (CG) of a vehicle. These frame systems are shown in figure 2.1, and they can switch around through Euler angle transformation.

Unlike most of the vehicle modeling works, we introduce the road frame system to accommodate the change of road angle. This road frame system is particularly useful because lots of vehicle motions are performed relative to the road surface, instead of a fixed point on earth. In other words, it is more effective to describe the vehicle dynamics in terms of the road frame than of the global frame.

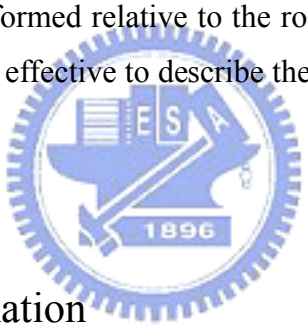

2.1.1 Euler Transformation

In this section, we will introduce two Euler transformations for 4 coordinate systems. First Euler transformation is shown in figure 2.2, and three Euler's angles ($\varepsilon, \theta, \phi$) are used to represent the coordinate relationship between the global frame and body frame. In the Euler transformation, yaw motion (ε) rotates along the vertical axis (z), pitch motion (θ) rotates along the lateral axis (y) and roll motion (ϕ) rotates along the longitudinal axis (x). Then, we can define the proper orthogonal rotation tensor (Q) such that the motion in the global frame can be transformed to the body frame by the following equations,

$$\begin{aligned} E^B &= Q \cdot E^G \\ &= Q_x \cdot Q_y \cdot Q_z \cdot E^G \end{aligned} \tag{2.1}$$

with $$Q_x = \begin{bmatrix} 1 & 0 & 0 \\ 0 & \cos\phi & \sin\phi \\ 0 & -\sin\phi & \cos\phi \end{bmatrix}$$

$$Q_y = \begin{bmatrix} \cos\theta & 0 & -\sin\theta \\ 0 & 1 & 0 \\ \sin\theta & 0 & \cos\theta \end{bmatrix}$$

$$Q_z = \begin{bmatrix} \cos\varepsilon & \sin\varepsilon & 0 \\ -\sin\varepsilon & \cos\varepsilon & 0 \\ 0 & 0 & 1 \end{bmatrix}$$

where $Q_{x,y,z}$ represents the transformation matrix from the global frame to the body frame. Therefore, we can describe the vehicle motion in the global frame, wheel frame, and body frame by Euler transformation.

Second Euler transformation is set between the global frame and the wheel frame to represent the road frame for the coordinate transformation. As shown in figure 2.3, we can describe the road curvatures by the three Euler angles (ε_{road}, ϕ_{road}, θ_{road}). Again, the proper orthogonal tensor (Q^{road}) is defined such that the motion in the global frame can be transformed to the road frame by the following equations,

$$\begin{aligned} E^{road} &= Q^{road} \cdot E^{G} \\ &= Q_{\varepsilon}^{road} \cdot Q_{\phi}^{road} \cdot Q_{\theta}^{road} \cdot E^{G} \end{aligned} \tag{2.2}$$

with $$Q_{\varepsilon}^{road} = \begin{bmatrix} \cos\varepsilon_{road} & \sin\varepsilon_{road} & 0 \\ -\sin\varepsilon_{road} & \cos\varepsilon_{road} & 0 \\ 0 & 0 & 1 \end{bmatrix}$$

$$Q_{\phi}^{road} = \begin{bmatrix} 1 & 0 & 0 \\ 0 & \cos\phi_{road} & \sin\phi_{road} \\ 0 & -\sin\phi_{road} & \cos\phi_{road} \end{bmatrix}$$

$$Q_{\theta}^{road} = \begin{bmatrix} \cos\theta_{road} & 0 & -\sin\theta_{road} \\ 0 & 1 & 0 \\ \sin\theta_{road} & 0 & \cos\theta_{road} \end{bmatrix}$$

where $Q_{\varepsilon,\phi,\theta}^{road}$ represents the transformation matrix from the global frame to the road frame.

Therefore, we can take these two Euler transformations to derive the vehicle motion in the following sections.

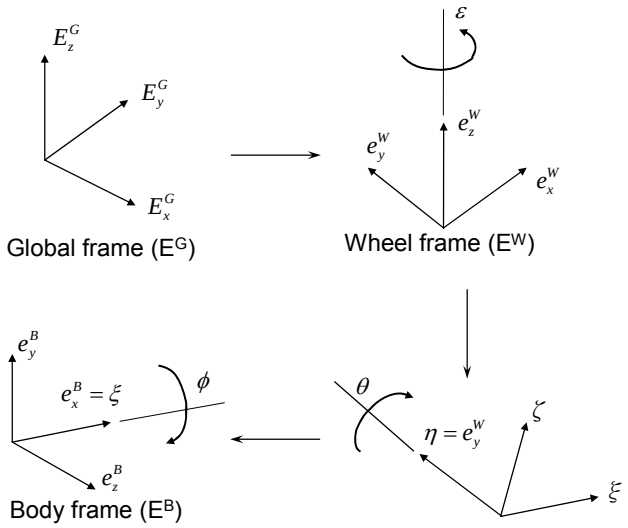

Figure 2.2 Diagram of Euler transformations from the global frame to the body frame

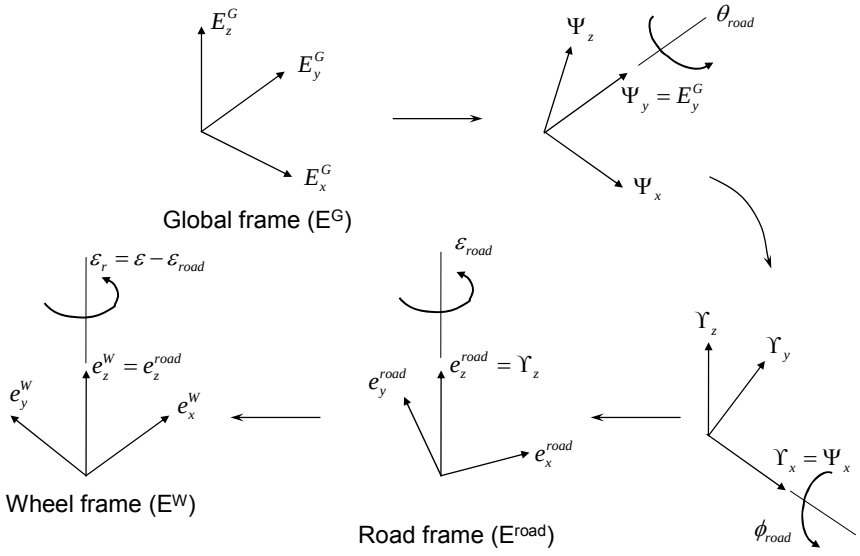

Figure 2.3 Diagram of Euler transformations from the global frame to the wheel frame

2.2 Sprung Mass System

Assuming the rigid body motion, as the free body diagrams shown in figure 2.4, the sprung mass clearly has six degree-of-freedoms, which are three rotational motions and three translational motions for the center of gravity (CG). These motions of the sprung mass are briefly described as follows.

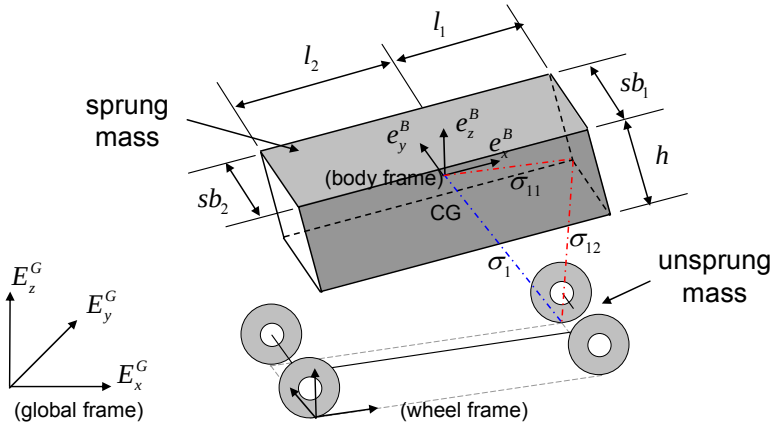

Figure 2.4 Free body diagrams of the vehicle

2.2.1 Vehicle Rotational Motion

The vehicle rotation dynamics can be conveniently written in equations in the coordinate that is rotated with the car (body frame) and then transformed back to the coordinate that is fixed to the earth (global frame) by the above-mentioned Euler's angles (ε , θ , ϕ) transformation. Hence, the angular velocity along three axes which rotated by Euler's angles can be expressed as follows,

$$\begin{aligned}
\omega_\phi &= Q_z \begin{bmatrix} \dot{\phi} \\ 0 \\ 0 \end{bmatrix} = \begin{bmatrix} 1 & 0 & 0 \\ 0 & \cos\phi & \sin\phi \\ 0 & -\sin\phi & \cos\phi \end{bmatrix} \begin{bmatrix} \dot{\phi} \\ 0 \\ 0 \end{bmatrix} = \begin{bmatrix} \dot{\phi} \\ 0 \\ 0 \end{bmatrix} \\
\omega_\theta &= Q_z Q_y \begin{bmatrix} 0 \\ \dot{\theta} \\ 0 \end{bmatrix} = \begin{bmatrix} 0 \\ \dot{\theta}\cos\phi \\ -\dot{\theta}\sin\phi \end{bmatrix} \\
\omega_\varepsilon &= Q_z Q_y Q_x \begin{bmatrix} 0 \\ 0 \\ \dot{\varepsilon} \end{bmatrix} = \begin{bmatrix} -\dot{\varepsilon}\sin\theta \\ \dot{\varepsilon}\cos\theta\sin\phi \\ \dot{\varepsilon}\cos\theta\cos\phi \end{bmatrix}
\end{aligned} \tag{2.3}$$

where $\omega_{\phi,\theta,\varepsilon}$ is the Euler angular velocity, and in these angular velocity, ω_{ε} rotates along the axis e_z^W, ω_{θ} rotates along the axis η, and ω_{ϕ} rotates along the axis e_x^B. Therefore, the vehicle angular rate and the vehicle angular acceleration can be expressed in terms of the Euler angle dynamics as follows:

$$\begin{aligned}\omega_x &= \dot{\phi} - \dot{\varepsilon}\sin\theta \\ \omega_y &= \dot{\theta}\cos\phi + \dot{\varepsilon}\cos\theta\sin\phi \\ \omega_z &= -\dot{\theta}\sin\phi + \dot{\varepsilon}\cos\theta\cos\phi\end{aligned} \tag{2.4}$$

$$\begin{aligned}\dot{\omega}_x &= \ddot{\phi} - \ddot{\varepsilon}\sin\theta - \dot{\varepsilon}\dot{\theta}\cos\theta \\ \dot{\omega}_y &= \ddot{\theta}\cos\phi + \ddot{\varepsilon}\cos\theta\sin\phi - \dot{\theta}\dot{\phi}\sin\phi - \dot{\varepsilon}\dot{\theta}\sin\theta\sin\phi + \dot{\varepsilon}\dot{\phi}\cos\theta\cos\phi \\ \dot{\omega}_z &= -\ddot{\theta}\sin\phi + \ddot{\varepsilon}\cos\theta\cos\phi - \dot{\theta}\dot{\phi}\cos\phi - \dot{\varepsilon}\dot{\theta}\sin\theta\cos\phi - \dot{\varepsilon}\dot{\phi}\cos\theta\sin\phi\end{aligned} \tag{2.5}$$

where $\omega_{x,y,z}$ is the vehicle angular rate represented in body frame.

The rotational motion of the vehicle body is to rotate about the roll center (RC), instead of the CG. Hence, the external moment consists of two parts: the angular momentum about the RC measured from the global frame and the angular momentum about the CG measured from the RC frame. Furthermore, because the RC frame is fixed in and move with the body frame, the angular velocity of the RC is the same with that of the CG. Therefore, using the well-known Euler equations of motion, one can presents the vehicle rotational dynamics as follows.

$$\left(\frac{dL}{dt}\right)_b + \omega \times L = M \tag{2.6}$$

where L is the angular momentum about the CG of the vehicle body, and M is the external moment about the CG of the vehicle body (M_x, M_y, M_z). Furthermore, we can expand the above equation in terms of the angular velocity in body frame.

$$\begin{aligned}M_x &= I_x\dot{\omega}_x - (I_y - I_z)\omega_y\omega_z \\ M_y &= I_y\dot{\omega}_y - (I_z - I_x)\omega_z\omega_x \\ M_z &= I_z\dot{\omega}_z - (I_x - I_y)\omega_x\omega_y\end{aligned} \tag{2.7}$$

where $I_{x,y,z}$ is the moment of inertial of the vehicle body. Then, from equations (2.4), (2.5), and (2.7), the vehicle rotational motion can be represented in terms of Euler's angles as follows,

$$\begin{aligned}
&\ddot{\phi} - \ddot{\varepsilon}\sin\theta = \dot{\varepsilon}\dot{\theta}\cos\theta + \\
&\qquad \frac{M_x}{I_x} - \frac{I_z - I_y}{I_x}\left(\dot{\theta}\cos\phi + \dot{\varepsilon}\cos\theta\sin\phi\right)\left(-\dot{\theta}\sin\phi + \dot{\varepsilon}\cos\theta\cos\phi\right) \\
&\ddot{\theta}\cos\phi + \ddot{\varepsilon}\cos\theta\sin\phi = \dot{\theta}\dot{\phi}\sin\phi + \dot{\varepsilon}\dot{\theta}\sin\theta\sin\phi - \dot{\varepsilon}\dot{\phi}\cos\theta\cos\phi + \\
&\qquad \frac{M_y}{I_y} - \frac{I_x - I_z}{I_y}\left(\dot{\phi} - \dot{\varepsilon}\sin\theta\right)\left(-\dot{\theta}\sin\phi + \dot{\varepsilon}\cos\theta\cos\phi\right) \\
&-\ddot{\theta}\sin\phi + \ddot{\varepsilon}\cos\theta\cos\phi = \dot{\theta}\dot{\phi}\cos\phi + \dot{\varepsilon}\dot{\theta}\sin\theta\cos\phi + \dot{\varepsilon}\dot{\phi}\cos\theta\sin\phi + \\
&\qquad \frac{M_z}{I_z} - \frac{I_y - I_x}{I_z}\left(\dot{\phi} - \dot{\varepsilon}\sin\theta\right)\left(\dot{\theta}\cos\phi + \dot{\varepsilon}\cos\theta\sin\phi\right)
\end{aligned} \tag{2.8}$$

Therefore, using the external moment discussed in the following section, we can obtain the information of Euler's angles, and then, can also obtain the vehicle angular velocity in body frame.

2.2.1.1 External Moment

The external moment contains the external forces and the associated moment arms. In order to match the above-mentioned Euler equations of motion, we will discuss the external moment on the CG of the vehicle body. Then, we can easily express the external moment as follows,

$$M = \sum_{i=1}^{4}\left(\sigma_i \times F_i^{body}\right) \tag{2.9}$$

where σ_i is the *i*th moment arms associated with the *i*th external force, and F_i^{body} is the *i*th external force in body frame.

2.2.1.2 External Forces

External forces of the vehicle body mainly come from tire forces and can be expressed as follows,

$$\sum_{i=1}^{4} F_i^{body} = \sum_{i=1}^{4} F_{xi}\cdot e_x^W + \sum_{i=1}^{4} F_{yi}\cdot e_y^W + \sum_{i=1}^{4} F_{zi}\cdot e_z^W \tag{2.10}$$

where $F_{x,y,zi}$ represents effective force in the wheel frame (e_x^W, e_y^W, e_z^W) from *i*th wheel in three directions, for i = 1~4 to represent a 4-wheels vehicle. However, the structure of tire forces does not suit to discuss in this section, and we will go into detail about this topic in section 2.3. Using the transformation matrix ($Q_x Q_y$), we can transform tire forces from the wheel frame to the body frame.

$$\begin{bmatrix} F_{xi}^{body} \\ F_{yi}^{body} \\ F_{zi}^{body} \end{bmatrix} = \begin{bmatrix} \cos\theta & 0 & -\sin\theta \\ \sin\theta\sin\phi & \cos\phi & \cos\theta\sin\phi \\ \sin\theta\cos\phi & -\sin\phi & \cos\theta\cos\phi \end{bmatrix} \begin{bmatrix} F_{xi} \\ F_{yi} \\ F_{zi} \end{bmatrix} = \begin{bmatrix} F_{xi}\cos\theta - F_{zi}\sin\theta \\ F_{xi}\sin\theta\sin\phi + F_{yi}\cos\phi + F_{zi}\cos\theta\sin\phi \\ F_{xi}\sin\theta\cos\phi - F_{yi}\sin\phi + F_{zi}\cos\theta\cos\phi \end{bmatrix} \quad (2.11)$$

Therefore, external forces in body frame are obtained, and in the next section, momentum arms in body frame will be introduced.

2.2.1.3 Momentum Arms

We take one of the momentum arms as the example for simplicity. As shown in figure 2.4, it will clearly find out where the momentum arm (σ_1, the blue dash line) is. This momentum arm is composed of two parts: σ_{11} and σ_{12} (the red dash lines), as shown in figure 2.4. We will separately discuss two momentum arms that locate in the different frames.

Firstly, the momentum arm (σ_{11}) locates in body frame. From the figure 2.4, we can intuitively set the CG of the vehicle body as the origin and write down the length of the momentum arm as vector term,

$$\sigma_{11} = l_1 e_x^B + \frac{sb_1}{2} e_y^B - \frac{h}{2} e_z^B \quad (2.12)$$

Secondly, the momentum arm (σ_{12}) locates in wheel frame. Again, we can also set the edge of the vehicle body as origin and write down the length of the momentum arm in vector term,

$$-(Z - z)e_z^W \quad (2.13)$$

where Z represents the height of the CG in the static situation, and z represents the height variation of the CG. However, the momentum arm (σ_{11}) with the vehicle pitch and roll

motion will induce the length variation of the momentum arm (σ_{12}). Here, we assume the length variation largely depends on the z axis in wheel frame for simplicity. Using the transformation matrix ($Q_x Q_y$), we can inversely transform the momentum arm (σ_{11}) from the body frame to the wheel frame.

$$\begin{bmatrix} *** \\ *** \\ Z_1^W \end{bmatrix} = \begin{bmatrix} \cos\theta & 0 & -\sin\theta \\ \sin\theta\sin\phi & \cos\phi & \cos\theta\sin\phi \\ \sin\theta\cos\phi & -\sin\phi & \cos\theta\cos\phi \end{bmatrix}^{-1} \begin{bmatrix} l_1 \\ \frac{sb_1}{2} \\ -\frac{h}{2} \end{bmatrix} \tag{2.14}$$

$$Z_1^W = \left(-l_1 \sin\theta + \frac{sb_1}{2}\cos\theta\sin\phi - \frac{h}{2}\cos\theta\cos\phi \right) e_z^W \tag{2.15}$$

where Z_1^W is the length variation at the front-left suspension in the wheel frame. Hence, using (2.13) and (2.15), we can obtain the partial momentum arm (σ_{12}) in wheel frame,

$$\sigma_{12} = \left(-l_1 \sin\theta + \frac{sb_1}{2}\cos\theta\sin\phi - \frac{h}{2}\cos\theta\cos\phi - (Z - z) \right) e_z^W \tag{2.16}$$

Two of partial momentum arms, as shown in equation (2.12) and (2.16), are derived in the different frames. However, the external forces ($F_{x,y,z}^{body}$), as shown in equation (2.11), are represented in the body frame. Therefore, we should transform the momentum arm to the body frame for calculation. Again, using the transformation matrix ($Q_x Q_y$), we can transform this momentum arm (σ_{12}) from the wheel frame to the body frame,

$$\begin{bmatrix} \cos\theta & 0 & -\sin\theta \\ \sin\theta\sin\phi & \cos\phi & \cos\theta\sin\phi \\ \sin\theta\cos\phi & -\sin\phi & \cos\theta\cos\phi \end{bmatrix} \begin{bmatrix} 0 \\ 0 \\ \sigma_{12} \end{bmatrix} = \begin{bmatrix} -\sigma_{12}\sin\theta \\ \sigma_{12}\cos\theta\sin\theta \\ \sigma_{12}\cos\phi\cos\theta \end{bmatrix} \cdot E^B \tag{2.17}$$

Then, the whole momentum arm (σ_1) in body frame can be composed of (2.12) and (2.17), shown as follows,

$$\sigma_1 = \begin{bmatrix} l_1 \\ \frac{sb_1}{2} \\ -\frac{h}{2} \end{bmatrix} - \begin{bmatrix} -\sigma_{12}\sin\theta \\ \sigma_{12}\cos\theta\sin\theta \\ \sigma_{12}\cos\phi\cos\theta \end{bmatrix} = \begin{bmatrix} l_1 + \sigma_{12}\sin\theta \\ \frac{sb_1}{2} - \sigma_{12}\cos\theta\sin\phi \\ -\frac{h}{2} - \sigma_{12}\cos\phi\cos\theta \end{bmatrix} \cdot E^B \tag{2.18}$$

In the same way, the other momentum arms (σ_2 , σ_3 , σ_4) can be calculated soon.

$$\sigma_2 = \begin{bmatrix} l_1 + \sigma_{22}\sin\theta \\ -\frac{sb_1}{2} - \sigma_{22}\cos\theta\sin\phi \\ -\frac{h}{2} - \sigma_{22}\cos\phi\cos\theta \end{bmatrix}$$

$$\sigma_3 = \begin{bmatrix} -l_2 + \sigma_{32}\sin\theta \\ -\frac{sb_2}{2} - \sigma_{32}\cos\theta\sin\phi \\ -\frac{h}{2} - \sigma_{32}\cos\phi\cos\theta \end{bmatrix} \qquad (2.19)$$

$$\sigma_2 = \begin{bmatrix} -l_2 + \sigma_{42}\sin\theta \\ \frac{sb_2}{2} - \sigma_{42}\cos\theta\sin\phi \\ -\frac{h}{2} - \sigma_{42}\cos\phi\cos\theta \end{bmatrix}$$

with $$\sigma_{22} = \left(-l_1\sin\theta - \frac{sb_1}{2}\cos\theta\sin\phi - \frac{h}{2}\cos\theta\cos\phi - (Z-z)\right)e_z^W$$

$$\sigma_{32} = \left(l_2\sin\theta - \frac{sb_2}{2}\cos\theta\sin\phi - \frac{h}{2}\cos\theta\cos\phi - (Z-z)\right)e_z^W$$

$$\sigma_{42} = \left(l_1\sin\theta + \frac{sb_2}{2}\cos\theta\sin\phi - \frac{h}{2}\cos\theta\cos\phi - (Z-z)\right)e_z^W$$

From the above two sections, we obtain two essential materials for the external moment, which are the external forces in body frame and the momentum arms in body frame. Therefore, we can derive the external moment in the next section.

2.2.1.4 External Moment Arrangement

Using equations (2.11), (2.18), and (2.19), the external moment, shown in equation (2.9), can be expanded as follows,

$$
\begin{aligned}
M = & \begin{bmatrix}
\frac{sb_1}{2}F_{z1}^{body} + \frac{h}{2}F_{y1}^{body} + \sigma_{12}F_{y1}\cos\theta \\
-\frac{sb_1}{2}F_{z2}^{body} + \frac{h}{2}F_{y2}^{body} + \sigma_{22}F_{y2}\cos\theta \\
-\frac{sb_2}{2}F_{z3}^{body} + \frac{h}{2}F_{y3}^{body} + \sigma_{32}F_{y3}\cos\theta \\
\frac{sb_2}{2}F_{z4}^{body} + \frac{h}{2}F_{y4}^{body} + \sigma_{42}F_{y4}\cos\theta
\end{bmatrix} e_x^B \\
& + \begin{bmatrix}
-l_1F_{z1}^{body} - \frac{h}{2}F_{x1}^{body} - \sigma_{12}\left(F_{x1}\cos\phi - F_{y1}\sin\theta\sin\phi\right) \\
-l_1F_{z2}^{body} - \frac{h}{2}F_{x2}^{body} - \sigma_{22}\left(F_{x2}\cos\phi - F_{y2}\sin\theta\sin\phi\right) \\
l_2F_{z3}^{body} - \frac{h}{2}F_{x3}^{body} - \sigma_{32}\left(F_{x3}\cos\phi - F_{y3}\sin\theta\sin\phi\right) \\
l_2F_{z4}^{body} - \frac{h}{2}F_{x4}^{body} - \sigma_{42}\left(F_{x4}\cos\phi - F_{y4}\sin\theta\sin\phi\right)
\end{bmatrix} e_y^B \\
& + \begin{bmatrix}
l_1F_{y1}^{body} - \frac{sb_1}{2}F_{x1}^{body} + \sigma_{12}\left(F_{x1}\sin\phi + F_{y1}\sin\theta\cos\phi\right) \\
l_1F_{y2}^{body} + \frac{sb_1}{2}F_{x2}^{body} + \sigma_{22}\left(F_{x2}\sin\phi - F_{y2}\sin\theta\cos\phi\right) \\
-l_2F_{y3}^{body} + \frac{sb_2}{2}F_{x3}^{body} + \sigma_{32}\left(F_{x3}\sin\phi - F_{y3}\sin\theta\cos\phi\right) \\
-l_2F_{y4}^{body} - \frac{sb_2}{2}F_{x4}^{body} + \sigma_{42}\left(F_{x4}\sin\phi - F_{y4}\sin\theta\cos\phi\right)
\end{bmatrix} e_z^B
\end{aligned}
\tag{2.20}
$$

Then, substituting (2.11), (2.18), and (2.19) into (2.20), the partial moments (M_x, M_y, M_z) can be expressed as follows,

$$
\begin{aligned}
M_x = & \frac{sb_1}{2}\left(F_{x1}\sin\theta\cos\phi - F_{y1}\sin\phi + F_{z1}\cos\theta\cos\phi\right) \\
& - \frac{sb_1}{2}\left(F_{x2}\sin\theta\cos\phi - F_{y2}\sin\phi + F_{z2}\cos\theta\cos\phi\right) \\
& - \frac{sb_2}{2}\left(F_{x3}\sin\theta\cos\phi - F_{y3}\sin\phi + F_{z3}\cos\theta\cos\phi\right) \\
& + \frac{sb_2}{2}\left(F_{x4}\sin\theta\cos\phi - F_{y4}\sin\phi + F_{z4}\cos\theta\cos\phi\right) \\
& + \frac{h}{2}\left(F_{x1}\sin\theta\sin\phi + F_{y1}\cos\phi + F_{z1}\cos\theta\sin\phi\right) \\
& + \frac{h}{2}\left(F_{x2}\sin\theta\sin\phi + F_{y2}\cos\phi + F_{z2}\cos\theta\sin\phi\right) \\
& + \frac{h}{2}\left(F_{x3}\sin\theta\sin\phi + F_{y3}\cos\phi + F_{z3}\cos\theta\sin\phi\right) \\
& + \frac{h}{2}\left(F_{x4}\sin\theta\sin\phi + F_{y4}\cos\phi + F_{z4}\cos\theta\sin\phi\right) \\
& + \left(-l_1\sin\theta + \frac{sb_1}{2}\cos\theta\sin\phi - \frac{h}{2}\cos\theta\cos\phi - \left(Z - z\right)\right)F_{y1}\cos\theta \\
& + \left(-l_1\sin\theta - \frac{sb_1}{2}\cos\theta\sin\phi - \frac{h}{2}\cos\theta\cos\phi - \left(Z - z\right)\right)F_{y2}\cos\theta \\
& + \left(l_2\sin\theta - \frac{sb_2}{2}\cos\theta\sin\phi - \frac{h}{2}\cos\theta\cos\phi - \left(Z - z\right)\right)F_{y3}\cos\theta \\
& + \left(l_2\sin\theta + \frac{sb_2}{2}\cos\theta\sin\phi - \frac{h}{2}\cos\theta\cos\phi - \left(Z - z\right)\right)F_{y4}\cos\theta
\end{aligned}
\tag{2.21}
$$

$$
\begin{aligned}
M_y = & -l_1\left(F_{x1}\sin\theta\cos\phi - F_{y1}\sin\phi + F_{z1}\cos\theta\cos\phi\right) \\
& - l_1\left(F_{x2}\sin\theta\cos\phi - F_{y2}\sin\phi + F_{z2}\cos\theta\cos\phi\right) \\
& + l_2\left(F_{x3}\sin\theta\cos\phi - F_{y3}\sin\phi + F_{z3}\cos\theta\cos\phi\right) \\
& + l_2\left(F_{x4}\sin\theta\cos\phi - F_{y4}\sin\phi + F_{z4}\cos\theta\cos\phi\right) \\
& - \frac{h}{2}\left(F_{x1}\cos\theta - F_{z1}\sin\theta\right) - \frac{h}{2}\left(F_{x2}\cos\theta - F_{z2}\sin\theta\right) \\
& - \frac{h}{2}\left(F_{x3}\cos\theta - F_{z3}\sin\theta\right) - \frac{h}{2}\left(F_{x4}\cos\theta - F_{z4}\sin\theta\right) \\
& - \left(-l_1\sin\theta + \frac{sb_1}{2}\cos\theta\sin\phi - \frac{h}{2}\cos\theta\cos\phi - \left(Z - z\right)\right)\left(F_{x1}\cos\phi - F_{y1}\sin\theta\sin\phi\right) \\
& - \left(-l_1\sin\theta - \frac{sb_1}{2}\cos\theta\sin\phi - \frac{h}{2}\cos\theta\cos\phi - \left(Z - z\right)\right)\left(F_{x2}\cos\phi - F_{y2}\sin\theta\sin\phi\right) \\
& - \left(l_2\sin\theta - \frac{sb_2}{2}\cos\theta\sin\phi - \frac{h}{2}\cos\theta\cos\phi - \left(Z - z\right)\right)\left(F_{x3}\cos\phi - F_{y3}\sin\theta\sin\phi\right) \\
& - \left(l_2\sin\theta + \frac{sb_2}{2}\cos\theta\sin\phi - \frac{h}{2}\cos\theta\cos\phi - \left(Z - z\right)\right)\left(F_{x4}\cos\phi - F_{y4}\sin\theta\sin\phi\right)
\end{aligned}
\tag{2.22}
$$

$$
\begin{aligned}
M_z = & \; l_1\left(F_{x1}\sin\theta\sin\phi + F_{y1}\cos\phi + F_{z1}\cos\theta\sin\phi\right) \\
& + l_1\left(F_{x2}\sin\theta\sin\phi + F_{y2}\cos\phi + F_{z2}\cos\theta\sin\phi\right) \\
& - l_2\left(F_{x3}\sin\theta\sin\phi + F_{y3}\cos\phi + F_{z3}\cos\theta\sin\phi\right) \\
& - l_2\left(F_{x4}\sin\theta\sin\phi + F_{y4}\cos\phi + F_{z4}\cos\theta\sin\phi\right) \\
& - \frac{sb_1}{2}\left(F_{x1}\cos\theta - F_{z1}\sin\theta\right) + \frac{sb_1}{2}\left(F_{x2}\cos\theta - F_{z2}\sin\theta\right) \\
& + \frac{sb_2}{2}\left(F_{x3}\cos\theta - F_{z3}\sin\theta\right) - \frac{sb_2}{2}\left(F_{x4}\cos\theta - F_{z4}\sin\theta\right) \\
& + \left(-l_1\sin\theta + \frac{sb_1}{2}\cos\theta\sin\phi - \frac{h}{2}\cos\theta\cos\phi - \left(Z - z\right)\right)\left(F_{x1}\sin\phi + F_{y1}\sin\theta\cos\phi\right) \\
& + \left(-l_1\sin\theta - \frac{sb_1}{2}\cos\theta\sin\phi - \frac{h}{2}\cos\theta\cos\phi - \left(Z - z\right)\right)\left(F_{x2}\sin\phi + F_{y2}\sin\theta\cos\phi\right) \\
& + \left(l_2\sin\theta - \frac{sb_2}{2}\cos\theta\sin\phi - \frac{h}{2}\cos\theta\cos\phi - \left(Z - z\right)\right)\left(F_{x3}\sin\phi + F_{y3}\sin\theta\cos\phi\right) \\
& + \left(l_2\sin\theta + \frac{sb_2}{2}\cos\theta\sin\phi - \frac{h}{2}\cos\theta\cos\phi - \left(Z - z\right)\right)\left(F_{x4}\sin\phi + F_{y4}\sin\theta\cos\phi\right)
\end{aligned}
\tag{2.23}
$$

The derivation of the vehicle rotational motion is complete here. Therefore, vehicle angular velocity presented in body frame can be obtained by Euler's angles.

2.2.2 Vehicle Translational Motion

Using Newton's equations, we can clearly express the linear motion for the CG of the vehicle body. However, we should check what terms the acceleration contains. Therefore, we can obtain the vehicle translation dynamics.

2.2.2.1 Newton's Equation

The vehicle translation dynamics can be conveniently written in equations by Newton's equation as follows:

$$\begin{aligned} m_{vehicle} \cdot a_x &= \sum F_{xi} \\ m_{vehicle} \cdot a_y &= \sum F_{yi} \\ m_{vehicle} \cdot a_z &= \sum F_{zi} - g \end{aligned} \tag{2.24}$$

where x, y, z represent longitudinal, lateral and vertical displacement of CG, respectively, F_i represents effective force from *i*th wheel in each direction, for *i* = 1~4 to represent a 4-wheels vehicle, $m_{vehicle}$ is the total vehicle mass from sprung mass and unsprung mass, and g is the earth gravity.

2.2.2.2 Acceleration

The acceleration contains not only linear acceleration along three axes, but also inertial acceleration induced by the angular velocity and angular acceleration. Therefore, the acceleration can be written down as follows,

$$\begin{aligned} \vec{a} &= \overrightarrow{a_0} + \vec{\omega} \times \left(\vec{\omega} \times \vec{r} \right) \\ &= \overrightarrow{a_0} + \vec{\omega} \times \vec{V} \\ &\cong \begin{bmatrix} \ddot{x} \\ \ddot{y} \\ \ddot{z} \end{bmatrix} + \begin{bmatrix} \dot{\phi} \\ \dot{\theta} \\ \dot{\varepsilon} \end{bmatrix} \times \begin{bmatrix} \dot{x} \\ \dot{y} \\ \dot{z} \end{bmatrix} \cong \begin{bmatrix} \ddot{x} - \dot{y}\dot{\varepsilon} \\ \ddot{y} + \dot{x}\dot{\varepsilon} \\ \ddot{z} \end{bmatrix} = \begin{bmatrix} a_x \\ a_y \\ a_z \end{bmatrix} \end{aligned} \tag{2.25}$$

where $\vec{a} = [a_x, a_y, a_z]^T$ represents the acceleration in each direction, $\vec{\omega} \cong [\dot{\phi}, \dot{\theta}, \dot{\varepsilon}]^T$ represents the angular velocity along each direction, and $\vec{V} = [\dot{x}, \dot{y}, \dot{z}]^T$ represents the velocity in each direction. Here, the vehicle angular velocity ($\omega_x, \omega_y, \omega_z$), shown in equation (2.4), contains many terms of Euler's angles. However, we assume the vehicle angular velocity is close to the Euler angular velocity ($\dot{\phi}, \dot{\theta}, \dot{\varepsilon}$), and two of the Euler angular velocity, ($\dot{\phi}, \dot{\theta}$) are smaller than the other angular velocity, ($\dot{\varepsilon}$). Hence, we only consider the acceleration induced by the vehicle yaw angular velocity ($\dot{\varepsilon}$), as shown in equation (2.25).

Therefore, substituting equation (2.25) into equation (2.24), we can write down the equations of the linear motion as follows,

$$
\begin{aligned}
m_{vehicle}(\ddot{x} - \dot{y}\dot{\varepsilon}) &= \sum F_{xi} \\
m_{vehicle}(\ddot{y} + \dot{x}\dot{\varepsilon}) &= \sum F_{yi} \\
m_{vehicle}(\ddot{z}) &= \sum F_{zi} - g
\end{aligned}
\tag{2.26}
$$

The derivation of the vehicle translational motion is complete here.

2.3 Unsprung Mass System

The unsprung mass, which consisted of axles, chassis, and four tires, is crucial to a full-car modeling. Its dynamic characteristics are described in various subsystems for expression clarity, which include wheel steering system, suspension system, tire model, wheel dynamics and road bank condition. The dynamics of these subsystems are first discussed individually and put back together via physical principles and Euler angle transformation.

2.3.1 Wheel Steering System

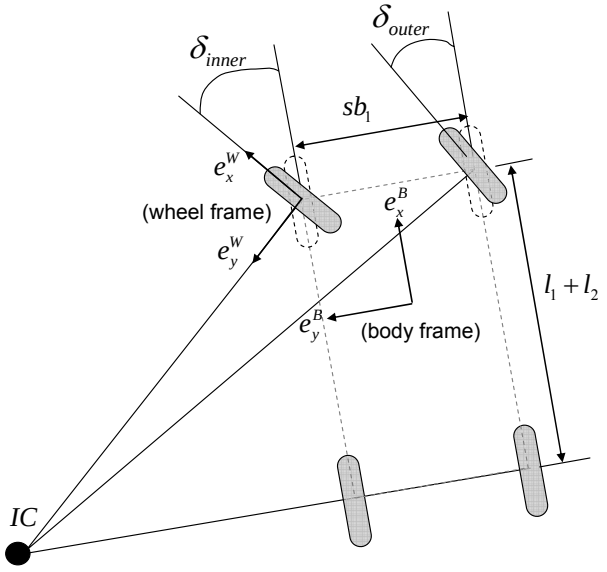

Figure 2.5 Ackerman principle

The Ackerman Steering principle is to ensure a vehicle can be smoothly cornering. As shown in figure 2.5, the vehicle, turning slickly around the instantaneous center (IC), has the

different angles at the outer and inner tire. This principle specifies the angle relations between steering wheel angle, inner tire angle and outer tire angle [9]. The equation from the simple geometry in figure 2.5 can be written as follows:

$$\cot\delta_{outer} - \cot\delta_{inner} = \frac{sb_1}{l_1 + l_2} \tag{2.27}$$

where δ_{outer} is the steering angle of the outer tire, δ_{inner} is the steering angle of the inner tire, sb_1 represents the front tread width, and $l_{1,2}$ represent the distance from the CG to the front/rear axle.

After each tire angle is specified, the adhesive force generated by tires [15] [16] can be transformed from the wheel frame to the body frame. These force outputs are then fed into equations (2.8) and (2.26) for further derivation.

$$\begin{aligned} F_{xi} &= F_{ai}\cos\delta_i - F_{bi}\sin\delta_i \\ F_{yi} &= F_{ai}\sin\delta_i + F_{bi}\cos\delta_i \end{aligned} \tag{2.28}$$

where δ_i is the steering angle of the *i*th tire, $F_{a,b}$ is the longitudinal/lateral tire force of the *i*th tire, for i = 1~4 to represent 4-wheels. Additionally, this full-car model is set front-wheel steer ($\delta_3 = \delta_4 = 0$).

2.3.2 Suspension Force

Without losing much generality, a spring-damper system is considered for the vehicle suspension system. Most of the suspension-modeling works assume linear operations. However this assumption is likely to be erroneous in rollover incidence since a rollover usually accompanied with suspensions lift-off on one end and reach compression limits on the other end. The suspension at the lift-off end generates force to balance its own wheel weight and produces no net force on the vehicle body. The suspension on the other end reaches its maximum compression limit and the output force gradually saturated. For these reasons, the spring coefficient is modified to be nonlinear to handle these extreme cases. From the figure 2.6, the equations of suspension force can be written as follows:

$$F_{zi} = KH_i + D_{damper}\dot{H}_i + m_{ui}g$$
$$z = \frac{1}{4}\sum H_i \tag{2.29}$$

with $K = C_1 e^{C_2(H_i - C_3)}$

$$H_i = \begin{cases} H_i, & for\ H_i \le -m_{ui}g/K \\ -m_{ui}g/K, & for\ H_i \le -m_{ui}g/K \end{cases}$$

where K represents spring stiffness coefficient; C_m, m = 1, 2, 3 for nonlinear spring stiffness modeling, D_{damper} represents damper coefficient, m_{zi} represents unsprung mass from each tire weight and H_i represents spring compression at *i*th wheel. Lastly, the mean value of the displacement from each suspension is the vertical displacement of the unsprung-mass system.

The calculation of the spring compression at each suspension mainly focuses on the height induced by the vehicle pitch and roll motion. As discussed before, this induced height has been shown in equation (2.16). However, when considering the equation (2.16), we set the origin at the edge of the vehicle body. At this moment, we should set the origin at the bottom of the suspension system, shown in figure 2.6. In this regard, we will not consider the height (Z) of the CG, because of concerning the spring compression. Therefore, the spring compression at each suspension can be written down as follows,

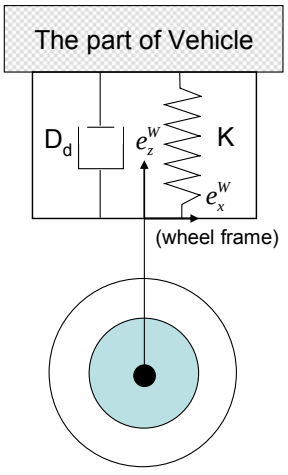

Figure 2.6 Diagram of the passive suspension system

$$H = \begin{bmatrix} H_1 \\ H_2 \\ H_3 \\ H_4 \end{bmatrix} = \begin{bmatrix} l_1 \sin\theta - \frac{sb_1}{2}\cos\theta\sin\phi + \frac{h}{2}\cos\theta\cos\phi - z \\ l_1 \sin\theta + \frac{sb_1}{2}\cos\theta\sin\phi + \frac{h}{2}\cos\theta\cos\phi - z \\ -l_2 \sin\theta + \frac{sb_2}{2}\cos\theta\sin\phi + \frac{h}{2}\cos\theta\cos\phi - z \\ -l_2 \sin\theta - \frac{sb_2}{2}\cos\theta\sin\phi + \frac{h}{2}\cos\theta\cos\phi - z \end{bmatrix} \tag{2.30}$$

Additionally, suspension forces will cause the deflection of tires and change the radius of tires. Therefore, we should consider this variation in radius for further derivation.

$$r_{ei} = r_i - \frac{F_{zi}}{K_{vertical}} \tag{2.31}$$

where r_{ei} is the effective rolling radius of *i*th tire, r_i is the real radius of *i*th tire, and $K_{vertical}$ is the tire vertical stiffness.

2.3.3 Nonlinear Tire Model

The study of the tire model in previous research can be classified into three approaches: empirical, physical, and hybrid model [17]. In this thesis, we use the hybrid model, which is named the magic formula tire model [15] [16], for its accuracy. The forces generated by the tire are obtained from the magic formula tire model and associated tire parameters, used in this simulation, are excerpted from Feng's dissertation [7]. This nonlinear tire model takes the vertical loads to identify tire parameters, and uses slip ratio, slip angle, and tire parameters to get tire forces. In this section, the construction of the nonlinear tire mode will be described.

2.3.3.1 Pacejka's Magic Formula Tire Model

From [15] [16], the magic formula tire model is shown as follows:

$$\begin{aligned} F_a &= D_x \sin\left\{C_x \tan^{-1}\left[B_x\lambda - E_x\left(B_x\alpha - \tan^{-1}\left(B_x\lambda\right)\right)\right]\right\} \\ F_b &= D_y \sin\left\{C_y \tan^{-1}\left[B_y\alpha - E_y\left(B_y\beta - \tan^{-1}\left(B_y\alpha\right)\right)\right]\right\} \end{aligned} \tag{2.32}$$

where $F_{a,b}$ represent the longitudinal/lateral adhesive force, λ is the slip ratio of the tire, α is the slip angle of the tire, and B, C, D, E represent the associated tire parameters.

Additionally, the slip ratio is defined as the respective speed difference between the tire and vehicle at the each side. The slip angle is defined as the respective angle difference between the tire and vehicle at the each side. These two physical quantities are both induced by the frictional coefficient of the road, and are the best suitable parameter of the tire force.

According to the magic formula, the tire longitudinal and lateral forces are functions of slip ratio, slip angle and tire parameters. Moreover, tire parameters change with vertical loads and thus they need to be calculated in real-time. Additionally, the tire "self-alignment torque" and "longitudinal-lateral force coupling" effect, mentioned in [15] [16], are neglected in this simulation for simplicity.

However, the lateral force has the other component, mentioned in [7], are also considered in this thesis. Hence, the total lateral force can be expressed as,

$$F_b = D_y \sin\left\{C_y \tan^{-1}\left[B_y\alpha - E_y\left(B_y\beta - \tan^{-1}\left(B_y\alpha\right)\right)\right]\right\} + \gamma\phi \tag{2.33}$$

where γ is the respective coefficients from the camber thrust, and ϕ is the Euler roll angle.. Additionally, the camber thrust is assumed linear respect to the Euler roll angle for simplicity [7].

2.3.3.2 Slip Ratio and Slip Angle

As discussed before, the slip ratio depends on the vehicle speed and the tire speed in the longitudinal direction. Hence, the slip ratio is expressed as follows,

$$\lambda_i = \frac{r_{ei}\omega_i - V_i\cos\alpha_i}{\max\{r_{ei}\omega_i, V_i\cos\alpha_i\}} \tag{2.34}$$

with
$$V_1 = (\dot{x} - \frac{sb_1}{2}\dot{\varepsilon})e_x^W + (\dot{y} + l_1\dot{\varepsilon})e_y^W$$
$$V_2 = (\dot{x} + \frac{sb_1}{2}\dot{\varepsilon})e_x^W + (\dot{y} + l_1\dot{\varepsilon})e_y^W$$
$$V_3 = (\dot{x} + \frac{sb_2}{2}\dot{\varepsilon})e_x^W + (\dot{y} - l_2\dot{\varepsilon})e_y^W$$
$$V_4 = (\dot{x} - \frac{sb_2}{2}\dot{\varepsilon})e_x^W + (\dot{y} - l_2\dot{\varepsilon})e_y^W$$

where r_{ei} is the effective rolling radius of the *i*th tire, ω_i is the *i*th tire angular velocity, and V_i is the vehicle speed at the *i*th side. Additionally, when choosing the tire speed ($r_{ei}\omega_i$) as

the denominator, it means the vehicle does the tracking maneuver. Furthermore, when choosing the vehicle speed ($V_i \cos\alpha_i$) as the denominator, it means the vehicle does the braking maneuver.

As discussed before, the slip angle value depends on the tire attitude and vehicle attitude. The tire attitude contains steering angle, sideslip angle, roll steer, kingpin inclination etc. However, in this thesis, the slip angle only considers the steering angle, sideslip angle, and roll steer. Therefore, the slip angle is expressed as follows,

$$\alpha_i = \delta_i - \tan^{-1}\beta_i - \kappa_i\phi \tag{2.35}$$

with $\beta_1 = (\dot{y} + l_1\dot{\varepsilon})(\dot{x} - \frac{sb_1}{2}\dot{\varepsilon})^{-1}$

$\beta_2 = (\dot{y} + l_1\dot{\varepsilon})(\dot{x} + \frac{sb_1}{2}\dot{\varepsilon})^{-1}$

$\beta_3 = (\dot{y} - l_2\dot{\varepsilon})(\dot{x} + \frac{sb_2}{2}\dot{\varepsilon})^{-1}$

$\beta_4 = (\dot{y} - l_2\dot{\varepsilon})(\dot{x} - \frac{sb_2}{2}\dot{\varepsilon})^{-1}$

where β_i is the side slip angle at *i*th tire, and κ_i is the roll steer coefficient. Additionally, we assume the roll steer angle, induced by the vehicle roll motion, is also linear respect to the Euler roll angle for simplicity [7].

2.3.4 Wheel Dynamics

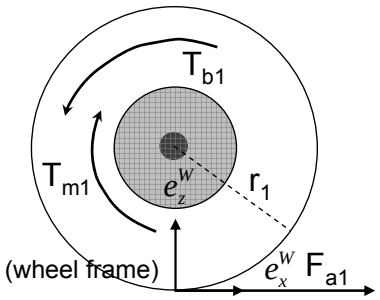

Figure 2.7 Diagram of front-wheel free-body

As shown in figure 2.7, the spinning wheels are accelerated by motor torque and decelerated by both braking torque and adhesive tire forces.

$$I_{wheel}\dot{\omega}_i = -r_i F_{ai} - T_{brake,i} + T_{motor,i} \tag{2.36}$$

where I_{wheel} represents moment of inertia of the tire, ω_i represents the angular rate of the each tire, r_i represents the effective rolling radius of the each tire, $T_{brake,i}$ represents the braking torque acting on the each tire, and $T_{motor,i}$ represents the motor torque acting on the each tire. Additionally, this full-car model is set front-wheel drive ($T_{motor,3} = T_{motor,4} = 0$). Thanks to the equation obtained for wheel dynamics, we are able to link wheel angular velocity with the power train system, braking system and adhesive tire force all together.

2.4 Road Condition

As shown in figure 2.8, the road bank condition, which include curves and slopes of roads, are introduced into the vehicle dynamics modeling by inserting a "road frame" in between the conventional "global frame" and "body frame".

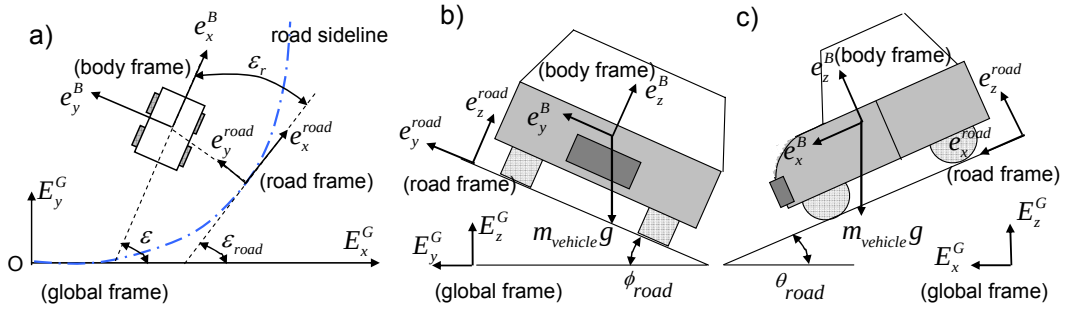

Figure 2.8 Vehicle motion in the three road conditions. a) the relationship between vehicle yaw angle (ε) and road yaw angle (ε_{road}), b) the vehicle motion on a slop, c) the vehicle motion on a downward

These road curvatures can be intuitively described by the three Euler angles (ε_{road}, ϕ_{road}, θ_{road}) for the coordinate transformation. Since the rollover incidence is declared by the vehicle roll angle relative to the road level, it is reasonable to express the vehicle dynamics in

the road frame, instead of global frame. Moreover, the gravity g is the only external force that is fixed to the global frame. Therefore, the forces induced by road bank angles and represented in road frame can be obtained as:

$$\begin{aligned}\begin{bmatrix} F_x^{road} \\ F_y^{road} \\ F_z^{road} \end{bmatrix} &= Q_\varepsilon^{road} Q_\phi^{road} Q_\theta^{road} \begin{bmatrix} 0 \\ 0 \\ -m_{vehicle} g \end{bmatrix} \\ &= \begin{bmatrix} -m_{vehicle} g\left(-\sin\theta_{road}\cos\varepsilon_{road} + \cos\theta_{road}\sin\phi_{road}\sin\varepsilon_{road}\right) \\ -m_{vehicle} g\left(\sin\theta_{road}\sin\varepsilon_{road} + \cos\theta_{road}\sin\phi_{road}\cos\varepsilon_{road}\right) \\ -m_{vehicle} g\cos\theta_{road}\cos\phi_{road} \end{bmatrix}\end{aligned} \tag{2.37}$$

with $$Q_\varepsilon^{road} = \begin{bmatrix} \cos\varepsilon_{road} & \sin\varepsilon_{road} & 0 \\ -\sin\varepsilon_{road} & \cos\varepsilon_{road} & 0 \\ 0 & 0 & 1 \end{bmatrix}$$

$$Q_\phi^{road} = \begin{bmatrix} 1 & 0 & 0 \\ 0 & \cos\phi_{road} & \sin\phi_{road} \\ 0 & -\sin\phi_{road} & \cos\phi_{road} \end{bmatrix}$$

$$Q_\theta^{road} = \begin{bmatrix} \cos\theta_{road} & 0 & -\sin\theta_{road} \\ 0 & 1 & 0 \\ \sin\theta_{road} & 0 & \cos\theta_{road} \end{bmatrix}$$

where $F_{x,y,z}^{road}$ represents effective forces induced by the road conditions and represented in the road frame and $Q_{\varepsilon,\phi,\theta}^{road}$ represents the transformation matrix from the global frame to the road frame.

The vehicle linear motion, as shown in equation (2.26), is derived in the body frame. However, the effective forces ($F_{x,y,z}^{road}$) are represented in the road frame. Therefore, we should transform the vehicle linear motion to the road frame for calculation. Again, using the transform matrix, the vehicle linear force, shown in equation (2.26), can be transformed to the road frame as follows,

$$\begin{bmatrix} \cos\varepsilon_r & \sin\varepsilon_r & 0 \\ -\sin\varepsilon_r & \cos\varepsilon_r & 0 \\ 0 & 0 & 1 \end{bmatrix}^{-1} \begin{bmatrix} F_{xi} \\ F_{yi} \\ 0 \end{bmatrix} = \begin{bmatrix} F_{xi}\cos\varepsilon_r - F_{yi}\sin\varepsilon_r \\ F_{xi}\sin\varepsilon_r + F_{yi}\cos\varepsilon_r \\ 0 \end{bmatrix} \tag{2.38}$$

where ε_r, shown in figure 2.8a, represents the relative yaw angle between the vehicle yaw angle (ε) and the road yaw angle (ε_{road}). Then, the acceleration, shown in the equation (2.25), can be rewritten as follows,

$$\overrightarrow{a^{road}} = \left(\ddot{x}^{road} - \dot{y}^{road}\dot{\varepsilon}_{road}\right)e_x^{road} + \left(\ddot{y}^{road} + \dot{x}^{road}\dot{\varepsilon}_{road}\right)e_y^{road} + \left(\ddot{z}^{road}\right)e_z^{road} \tag{2.39}$$

where $\overrightarrow{a^{road}}$ represents the acceleration of CG in road frame, and $(x, y, z)^{road}$ represent longitudinal, lateral, and vertical displacement of CG in road frame. Therefore, using equations (2.37), (2.38), and (2.39) by Newton's equation, we can rewrite the vehicle linear motion in road frame as follows,

$$\begin{aligned} m_{vehicle}\left(\ddot{x}^{road} - \dot{y}^{road}\dot{\varepsilon}_{road}\right) &= \sum F_{xi}\cos\varepsilon_r - \sum F_{yi}\sin\varepsilon_r + F_x^{road} \\ m_{vehicle}\left(\ddot{y}^{road} + \dot{x}^{road}\dot{\varepsilon}_{road}\right) &= \sum F_{xi}\sin\varepsilon_r + \sum F_{yi}\cos\varepsilon_r + F_y^{road} \\ m_{vehicle}\ddot{z}^{road} &= \sum F_{zi} + F_z^{road} \end{aligned} \tag{2.40}$$

Additionally, the road yaw rate ($\dot{\varepsilon}_{road}$) can be approximated by the vehicle longitudinal velocity in road frame and the curvature of the road centerline [13]. Hence, the road yaw rate can be approximated as follows,

$$\dot{\varepsilon}_{road} \cong \dot{x}^{road}\rho \tag{2.41}$$

The full-car modeling discussed in this paper is thus completed. The validation of this full car model will be discussed in the section 2.6.

2.5 Summary

Here, we summarize the main function of the full-car model for convenience. Using equations (2.36) and (2.40), we can get vehicle translation dynamics and associated equations, as follows,

$$\begin{aligned} m_{vehicle}\left(\ddot{x}^{road} - \dot{y}^{road}\dot{\varepsilon}_{road}\right) &= \sum F_{xi}\cos\varepsilon_r - \sum F_{yi}\sin\varepsilon_r + F_x^{road} \\ m_{vehicle}\left(\ddot{y}^{road} + \dot{x}^{road}\dot{\varepsilon}_{road}\right) &= \sum F_{xi}\sin\varepsilon_r + \sum F_{yi}\cos\varepsilon_r + F_y^{road} \\ m_{vehicle}\ddot{z} &= \sum F_{zi} + F_z^{road} \\ I_{wheel}\dot{\omega}_i &= -r_i F_{ai} - T_{brake,i} + T_{motor,i} \end{aligned} \tag{2.42}$$

Then, taking equations (2.28), (2.29), (2.32), (2.33), and (2.37) as the assistance, the vehicle linear motion can be clearly expressed.

Using the equation (2.9), we can get the vehicle rotational dynamics, as follows,

$$\begin{aligned}
&\ddot{\phi} - \ddot{\varepsilon}\sin\theta = \dot{\varepsilon}\dot{\theta}\cos\theta + \\
&\qquad \frac{M_x}{I_x} - \frac{I_z - I_y}{I_x}\left(\dot{\theta}\cos\phi + \dot{\varepsilon}\cos\theta\sin\phi\right)\left(-\dot{\theta}\sin\phi + \dot{\varepsilon}\cos\theta\cos\phi\right) \\
&\ddot{\theta}\cos\phi + \ddot{\varepsilon}\cos\theta\sin\phi = \dot{\theta}\dot{\phi}\sin\phi + \dot{\varepsilon}\dot{\theta}\sin\theta\sin\phi - \dot{\varepsilon}\dot{\phi}\cos\theta\cos\phi + \\
&\qquad \frac{M_y}{I_y} - \frac{I_x - I_z}{I_y}\left(\dot{\phi} - \dot{\varepsilon}\sin\theta\right)\left(-\dot{\theta}\sin\phi + \dot{\varepsilon}\cos\theta\cos\phi\right) \\
&-\ddot{\theta}\sin\phi + \ddot{\varepsilon}\cos\theta\cos\phi = \dot{\theta}\dot{\phi}\cos\phi + \dot{\varepsilon}\dot{\theta}\sin\theta\cos\phi + \dot{\varepsilon}\dot{\phi}\cos\theta\sin\phi + \\
&\qquad \frac{M_z}{I_z} - \frac{I_y - I_x}{I_z}\left(\dot{\phi} - \dot{\varepsilon}\sin\theta\right)\left(\dot{\theta}\cos\phi + \dot{\varepsilon}\cos\theta\sin\phi\right)
\end{aligned} \tag{2.43}$$

Then, taking equations (2.21), (2.22), and (2.23) as the assistance, the vehicle rotational motion can be clearly expressed.

2.6 Full-Car Model Validation

Now, we can not verify the validation of this full-car model, as result of the enormous experimental data. The production of the detail experimental data is needed time and cost. However, we are unable to find that this detail data is available. Therefore, the validation of this full car model will be verified by experimental data in future, if this detail data is in hand.

2.7 Conclusions

The developed nonlinear vehicle model, contained 21 system orders, is addressed in this chapter. Using Euler transformation, the relationship between dynamic frames is obtained, and then, sprung mass system and unsprung mass system can be incorporated. Additionally, we bring the road condition into the full-car model to obtain the vehicle dynamics induced by the road conditions and the vehicle roll angle with respect to the road surface. In this way, the full-car model presents more accurate simulation with the real vehicle. Furthermore, the derivation of this full-car model does not aim at some special kind of the vehicle. Therefore,

this methodology can be widely applied to four-wheel vehicles with different dynamic characteristics.

Chapter 3

System Observability of Full-Car Model

The states observability matrix can reveal the connections between system states and system outputs. Therefore, it is possible to employ this technique to discover the connections between each vehicle dynamics. Owing to the conventional observability matrix is inadequate for the vehicle rollover dynamics, we proposed a novel nonlinear observability matrix and, based on this matrix, the feasibility of neglecting vehicle pitch motions is discussed.

The unsuitability of the conventional observability matrix is described briefly in section 3.1. Under our demands, a novel observability matrix is proposed in section 3.2. Based on the simulation results, as shown in section 3.3, the integrated yaw-roll model is developed in section 3.4.

3.1 Nonlinear Observability Matrix

Most of the conventional observability matrix techniques discuss the system observability around equilibrium points [30]. They need lots of math derivations but are only applicable to a small operation range. The rollover incidence encounters a large roll angle variation and 21 system states. Therefore, it is impractical to construct a nonlinear observability matrix based on conventional methods.

Hahn J. and Edgar T. [11] proposed a new covariance matrix for the observability of nonlinear systems. This approach computes the observability grammian around system equilibrium points by applying perturbations on states initial conditions. And next, the observability grammian matrix corresponding to each initial condition is summed up, which makes it a covariance matrix in essence. This approach employs the concept of covariance matrix for the system observability. Unfortunately, it is only suitable for the small operation range.

3.2 Novel Observability Matrix along a Trajectory

Extended from the covariance matrix discussed previously [11], we proposed a novel system observability matrix that is applicable to a nonlinear system with a large operation range. In this approach, the observability grammian in [11] was replaced with the states covariance matrix. Furthermore, the calculation of states covariance matrix is performed along a trajectory, instead of at equilibrium points.

The proposed states covariance matrix along a trajectory can be calculated by the following steps.

1. Choose a trajectory of interest and along this trajectory, many distinct operation points are specified. These operation points are treated as the states initial conditions for simulation later on.
2. The perturbations are applied to each operation point as the initial conditions for numerical simulations. States covariance matrix can be calculated for each operation point.
3. Repeat the Step 2 for each operation point along the trajectory.
4. State covariance matrix obtained from each operation point is summed up and normalized for the final outcome.

This approach takes advantage of computer computation power to replace intensive math derivation, which makes it particularly suitable for a complicated nonlinear system with a wide operation range. However, the development of this method is not fully completed yet. More theoretical work is still on the way to ensure its feasibility.

3.3 Negligence of Pitch Motions

Table 3.1 shows the covariance matrix of the system along a stable trajectory. When comparing the numbers shown in “roll angle” column, we find relative small values in pitch motion and vertical motion, which imply that these two motions have less effect on the roll angle. The vertical motion can not be neglected in this case because it does play an important role of the CG lifting in a rollover incidence. The simulation fails to indicate its importance because the trajectory in this simulation is a stable one and does not involve much vertical motion. Therefore, if the order reduction must be made to the vehicle system, the vehicle pitch motion should be firstly considered.

	~	ε	$\dot{\varepsilon}$	θ	$\dot{\theta}$	ϕ	$\dot{\phi}$	~
x		0.0716	0.0503	-0.1112	-0.0343	0.0658	-0.0084	
$\dot{x}$		0.0072	0.0647	-0.0596	-0.0517	0.3201	-0.0288	
y		-0.2036	0.1784	0.1091	-0.0396	0.2200	0.0146	
$\dot{y}$		-0.3204	-0.0339	0.1580	-0.0385	0.1203	0.0598	
z		0.0563	0.1083	-0.8329	0.0077	0.0138	-0.0010	
$\dot{z}$		-0.0156	-0.0115	0.0070	-0.8555	0.0267	0.0756	
ε		1	0.1372	-0.2161	0.0272	0.0535	-0.0314	
$\dot{\varepsilon}$		0.1372	1	-0.1628	0.0213	0.0980	0.1574	
θ		-0.2161	-0.1628	1	-0.0189	0.0372	-0.0140	
$\dot{\theta}$		0.0272	0.0213	-0.0189	1	-0.0211	-0.0514	
ϕ	~	0.0535	0.0980	0.0372	-0.0211	1	0.0035	~
$\dot{\phi}$	~	-0.0314	0.1574	-0.0140	-0.0514	0.0035	1	~
$\dot{\varepsilon}_{road}$		-0.0076	0.0547	0.0977	-0.0153	0.0202	-0.0012	
ω_1		-0.2016	-0.2075	0.1914	0.0576	-0.0586	-0.0267	
ω_2		-0.2453	-0.1590	0.2494	0.0332	0.1266	0.0465	
ω_3		-0.1213	-0.0261	0.0383	0.0238	0.1578	0.0867	
ω_4		-0.3126	-0.2553	0.2106	0.0315	-0.1380	-0.0782	
H_1		0.1301	0.1468	0.1392	-0.1149	-0.2464	0.1154	
H_2		-0.1569	-0.1761	0.3201	-0.0898	0.2468	-0.0638	
H_3		0.4227	0.3330	-0.2791	-0.0034	0.4001	0.0164	
H_4		-0.4187	-0.3284	0.2091	0.0288	-0.4052	-0.0023	

Table 3.1 States covariance matrix in partial part.
(subscript 1: front-left side, 2: front-right side, 3: rear-right side, and 4: rear-left side)

3.4 Integrated Yaw-Roll Model

To obtain a simplified vehicle model, the vehicle pitch motion is neglected from the full-car model. The vehicle pitch motion (ω_y), as shown in equation (2.4), contains many terms other than Euler pitch angle (θ). However, we chose to neglect the Euler angle (θ), instead of the vehicle pitch angular velocity (ω_y), for simplicity for now. From equations (2.8), rotational dynamics of the full-car model can be deduced to the following.

$$\begin{aligned}
\ddot{\phi} &= \frac{M_x}{I_x} - \frac{I_z - I_y}{I_x}\left(\dot{\varepsilon}^2 \sin\phi\cos\phi\right) \\
\ddot{\varepsilon} &= \left(\frac{M_y}{I_y} - \frac{I_x - I_z}{I_y}\left(\dot{\phi}\dot{\varepsilon}\cos\phi\right)\right)\sin\phi + \left(\frac{M_z}{I_z} - \frac{I_y - I_x}{I_z}\left(\dot{\phi}\dot{\varepsilon}\sin\phi\right)\right)\cos\phi
\end{aligned} \tag{3.1}$$

The simplified vehicle model, with equations (3.1) for rotational dynamics, is named “integrated yaw-roll model” in this thesis. Additionally, the integrated yaw-roll model is considered as the real vehicle in this thesis. In the following section, the construction of the vehicle rollover prediction system will be based on this integrated yaw-roll model.

Chapter 4

Vehicle Rollover Prediction System

The proposed prediction system manages to incorporate an observer-based estimator. However, it is extremely difficult to construct a nonlinear observer for the full-car model, even for the integrated yaw-roll model. Owing to that, we proposed a novel separated yaw-roll model to reduce the intensive math derivation in the subsequent observer design. Furthermore, two observers work with suitable sensor measurements and compute in the ADI-like scheme. With this separated yaw-roll model and this switching observer scheme, we are able to estimate every vehicle states accurately. Additionally, the stability and convergence analysis of this switching scheme is also represented in this thesis.

As discussed before, the response of a dynamic system can be well described by a precise system model and associated initial conditions. In this thesis, we took the integrated yaw-roll model to accompany with the real-time vehicle states, which are estimated by the switching observer scheme. Therefore, we are able to correctly predict vehicle states in the future time. Additionally, this prediction method presents a strong evidence for a rollover occurrence.

Section 4.1 represents the separated yaw-roll model. The organization of the switching observer scheme is introduced in section 4.2, and the stability and convergence of that is presented in the next section. The suitable sensor and the suitable nonlinear observer are chosen in section 4.4 and 4.5. In the last section, the procedure of this whole system will be described briefly.

4.1 Separated Yaw-Roll Model

The novel separated yaw-roll model was obtained by breaking the integrated yaw-roll model into two subsystems, while preserving all the dynamics in the integrated yaw-roll model. As shown in the integrated yaw-roll model, Appendix A, the lateral force is present in both yaw dynamics and roll dynamics. To avoid the same states appearing in two sub-models, the lateral dynamics is ascribed to one model and the resulting lateral acceleration is

considered as the input to another model. With these arrangements, the integrated yaw-roll model is readily to be broken into two sub-models which are named “yaw model” and “roll model” in this thesis.

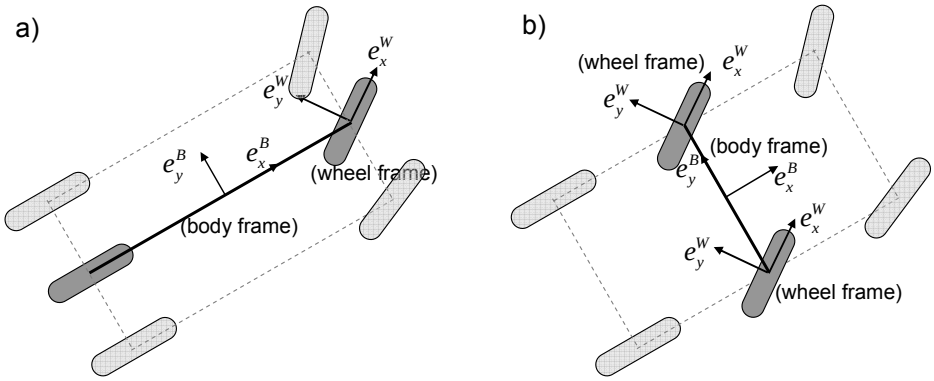

Figure 4.1 Comparison of the full-car model and separated yaw-roll model. a) diagram of the full-car model (in the light gray) and the yaw model (in the dark gray) b) diagram of the full-car model (in the light gray) and the roll model (in the dark gray)

4.1.1 Vehicle Yaw Model

The vehicle yaw model contains four degree-of-freedoms, which are longitudinal dynamics, lateral dynamics, yaw dynamics and wheel angular rate. The steering wheel angle, motor torque and brake torque, which originally considered as inputs to the integrated yaw-roll model, are treated as inputs to the yaw model. From some assumptions shown as followings, we can extract the vehicle yaw model from the integrated yaw-roll model.

- As discussed before, the Euler pitch angle (θ) and Euler pitch rate ($\dot{\theta}$) are neglected.
- The vehicle states associated with the vehicle roll model are considered as inputs to the vehicle yaw model.
- With neglecting the vehicle pitch motion, we are able to consider only two tires (front and rear tires) in the integrated yaw-roll model for the vehicle yaw modeling.

- From the 3rd assumption, we consider to set two imaginary tires, which locate individually in the middle of axles, as shown in figure 4.1a.
- From the 4th assumption, variables of imaginary tires, such as the tire slip ratio, tire slip angle, tire steering angle, etc., are set the mean value of left and right tires, which originate from the full-car model.
- From the 4th assumption, the geometry parameter, the tread width of the vehicle, is set as zero. ($sb_1 = sb_2 = 0$)

According to above-mentioned assumptions and equations (2.40) and (3.1), the dynamic equations of the yaw model are rearranged as follows:

$$\begin{aligned}
\ddot{\varepsilon} &= \left(\frac{M_y}{I_y} - \frac{I_x - I_z}{I_y} \left(\dot{\phi}\dot{\varepsilon} \cos\phi \right) \right) \sin\phi + \left(\frac{M_z}{I_z} - \frac{I_y - I_x}{I_z} \left(\dot{\phi}\dot{\varepsilon} \sin\phi \right) \right) \cos\phi \\
m_{vehicle} \left(\ddot{x}^{road} - \dot{y}^{road} \dot{\varepsilon}_{road} \right) &= \sum F_{xi} \cos\varepsilon_r - \sum F_{yi} \sin\varepsilon_r + F_x^{road} \\
m_{vehicle} \left(\ddot{y}^{road} + \dot{x}^{road} \dot{\varepsilon}_{road} \right) &= \sum F_{xi} \sin\varepsilon_r + \sum F_{yi} \cos\varepsilon_r + F_y^{road}
\end{aligned} \tag{4.1}$$

with

$$\begin{aligned}
M_y &= -l_1 \left(F_{y1} \sin\phi + F_{z1} \cos\phi \right) + l_2 \left(-F_{y2} \sin\phi + F_{z2} \cos\phi \right) \\
&\quad - \frac{h}{2} \left(F_{x1} + F_{x2} \right) - \left(-\frac{h}{2} \cos\phi - (Z - z) \right) \left(F_{x1} \cos\phi + F_{x2} \cos\phi \right) \\
M_z &= l_1 \left(F_{y1} \cos\phi + F_{z1} \sin\phi \right) - l_2 \left(F_{y2} \cos\phi + F_{z2} \sin\phi \right) \\
&\quad + \left(-\frac{h}{2} \cos\phi - (Z - z) \right) \left(F_{x1} \sin\phi + F_{x2} \sin\phi \right)
\end{aligned}$$

where the subscripts of tire forces (F_i), “1” and “2”, represent the front and rear of two imaginary tires. Then, the derivation of the yaw model is competed.

4.1.2 Vehicle Roll Model

The roll model contains three degree-of-freedoms, which are vertical dynamics, roll dynamics and suspension dynamics. The lateral acceleration is treated as the input to the roll model.

- As discussed before, the Euler pitch angle (θ) and Euler pitch rate ($\dot{\theta}$) are neglected.

- The vehicle states associated with the vehicle yaw model are considered as inputs to the vehicle roll model.
- With neglecting the vehicle pitch motion, we are able to consider only two tires (left and rear tires) in the integrated yaw-roll model for the vehicle roll modeling.
- From the 3rd assumption, we consider to set two imaginary tires, which locate in the middle of right end and in the middle of left end, as shown in figure 4.1b.
- From the 4th assumption, the nonlinear spring coefficient of the vehicle roll model is modified two times stiffer than that of the full-car model.
- From the 4th assumption, the geometry parameter, the wheelbase length of the vehicle, is set as zero. ($l_1 = l_2 = 0$)

According to above-mentioned assumptions and equations (2.40) and (3.1), the dynamic equations of the roll model are rearranged as follows:

$$\begin{aligned} \ddot{\phi} &= \frac{M_x}{I_x} - \frac{I_z - I_y}{I_x}\left(\dot{\varepsilon}^2 \sin\phi\cos\phi\right) \\ m_{vehicle}\ddot{z} &= \sum F_{zi} + F_z^{road} \end{aligned} \tag{4.2}$$

with $$M_x = F_{z1}\left(\frac{sb_1}{2}\cos\phi + \frac{h}{2}\sin\phi\right) + F_{z2}\left(-\frac{sb_1}{2}\cos\phi + \frac{h}{2}\sin\phi\right) + \left(-(Z-z)\right)\left(F_{y1} + F_{y2}\right)$$

where the subscripts of tire forces (F_i), "1" and "2", represent the left and right of two imaginary tires. Then, the derivation of the roll model is competed.

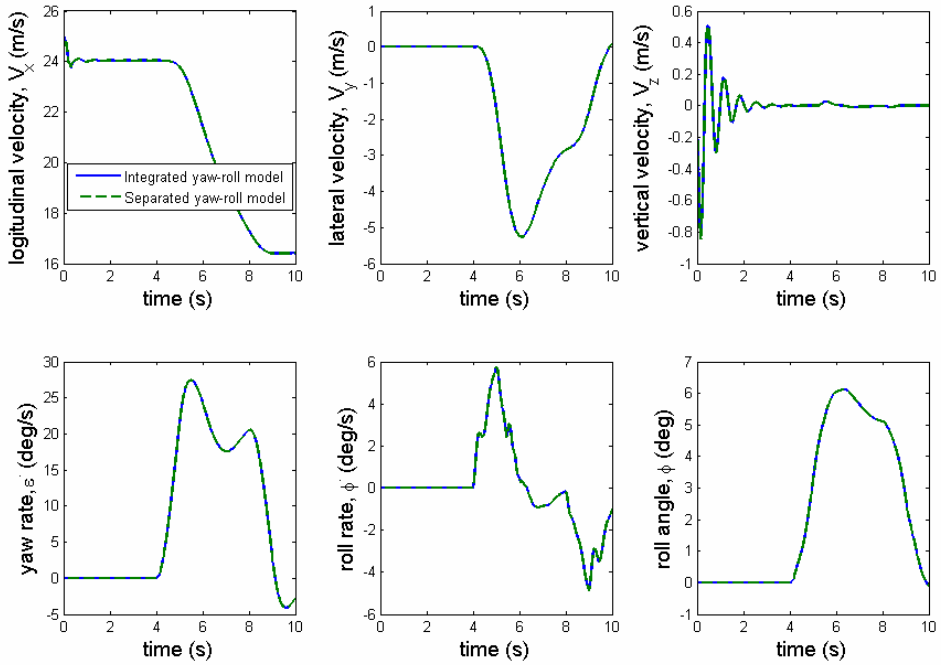

Figure 4.2 Dynamic responses of two models (the integrated yaw-roll model and the separated yaw-roll model) in the general case

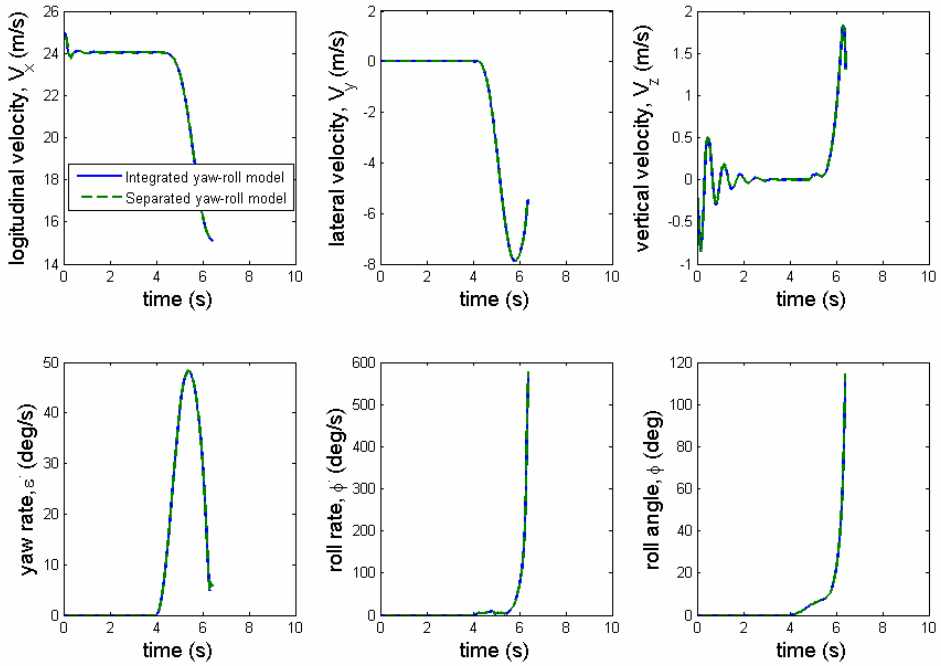

Figure 4.3 Dynamic responses of two models (the integrated yaw-roll model and the separated yaw-roll model) in the rollover case

4.1.3 Separated Yaw-Roll Model Validation

The validation of the separated yaw-roll model should be verified by the experimental data. As discussed before, we are unable to find the available data of the vehicle. Owing to that, we assume the integrated yaw-roll model has the accurate dynamic maneuver. Then, we design two simple driving maneuvers to compare with the dynamic response of the integrated yaw-roll model and the separated yaw-roll model. The comparison of simulation results will provide the evidence for the feasibility of the separated yaw-roll model.

In figure 4.2 and 4.3, the plot is arranged in the following order: longitudinal velocity in the upper left, lateral velocity in the upper middle, vertical velocity in the upper right, yaw rate in the lower left, roll rate in the lower middle, and roll angle in the lower right. Furthermore, the integrated yaw-roll model outputs are drawn in solid-blue lines, and the separated yaw-roll model outputs are drawn in dash-green lines.

As shown in figure 4.2 and 4.3, two dynamic responses are going in the same maneuver. Therefore, with these two simulation results, we can verify the validation of the separated yaw-roll model. Additionally, in the next section, we will use mathematical proof to show the stability of the separated yaw-roll model, and obtain the other evidence for the validation.

4.2 Switching Observer Scheme

After obtaining two subsystems for the separated yaw-roll model, the observer is constructed for each subsystem, respectively. These two observers work under a “switching scheme” in each simulation time step, which means, holding one subsystem when the other subsystem is doing the calculation. Although the separated yaw-roll model and integrated yaw-roll model possess the same system dynamics, the observer construction is indeed a lot simpler for the separated yaw-roll model accompanied with switching observer scheme.

4.2.1 Error Source

As discussed before, the proposed separated yaw-roll model is doing a switching scheme similar to conventional ADI methods. Therefore, same as the ADI method, the pertinent error can be attributed to two sources: switching time step error and round-off error [14].

The switching time step error mainly comes from the deviation generated by the high frequency content of the dynamic model, and this deviation propagates from one computation phase to another computation phase [14]. The round-off error is due to the discretization error and the digitization error [25]. The discretization error comes from the numerical approximation of a continuous-time function, which is needed for the computer numerical processing, and the digitization error comes from the finite length of digits. Therefore, the switching time step error largely depends on the switching time between two phases, and the round-off error largely depends on the computer hardware setup and the numerical method utilized to approximate a continuous-time differential equation.

In this thesis, we discussed the stability of this switching computation scheme for two cases. One employed "explicit Euler method" and the other one employed "Runge-Kutta method" as the accompanied numerical methods. At the end, the "Runge-Kutta method" is adopted for the vehicle rollover computer simulation in this thesis.

4.2.2 Preliminaries for the Stability Analysis of Switching Computation Scheme

Consider a nonlinear ordinary differential equation shown below.

$$\dot{x} = F(x(t)) \tag{4.3}$$

where $x \in \Re^n$, $F : \Re^n \to \Re^n$, and $0 \le t \le T$. The above equation can stand for many nonlinear autonomous systems at the finite time. By separating the states into two groups, we can break down a complicated nonlinear differential equation into two sets of differential equations.

$$F(x(t)) = F_1(x_1(t), x_2(t)) + F_2(x_1(t), x_2(t)) \tag{4.4}$$

where $x(t) = [x_1(t)\ \ x_2(t)]^T$, $x_1 \in \Re^m$, $x_2 \in \Re^{n-m}$, $F_1 : \Re^n \to \Re^m$ and $F_2 : \Re^n \to \Re^{n-m}$. Instead of using equation (4.3), the exact states values can be obtained from the following equation.

$$\begin{aligned} x_{1,n+1} &= x_{1,n} + \int_{t_n}^{t_{n+1}} F_1\big(x_1(t),\, x_2(t)\big)\, dt \\ x_{2,n+1} &= x_{2,n} + \int_{t_n}^{t_{n+1}} F_2\big(x_1(t),\, x_2(t)\big)\, dt \end{aligned} \tag{4.5}$$

where $x_i(t)$ is the states value at time t, $x_{i,n}$ represents the value of $x_i(t)$ at time $t = t_n$, $x_{i,n+1}$ represents the value of $x_i(t)$ at time $t = t_{n+1}$, $t_{n+1} = t_n + \tau$, and τ is the switching time interval. One thing to be noted, up to this point, we have not made any approximation or simplification for the differential equation calculation.

In this thesis, we solve equation (4.5) by an ADI-like method in order to estimate the system (4.3). Following the ADI-like method, two simpler functions can be seen as two space dimensions, and operated in the switching scheme to simulate this system. Additionally, this method reveals that the computational process activates alternatively in one dimension, and is called the locally one-dimensional (LOD) method. The link between the ADI-like method and the LOD method can govern step-by-step convergence stability for this system.

4.2.3 Stability Analysis for "Explicit Euler Method" Approximation

In order for computers to calculate above differential equations, we need to approximate the continuous-time function and integral operation by suitable numerical methods. Here, we use a simple "explicit Euler method" to approximate equation (4.5) as to focus on the switching computation scheme for the stability analysis work. At the end of this section, we shall show that the local deviation between solutions, obtained from explicit Euler method accompanied with switching computation scheme and from explicit Euler method without switching scheme, decreases as time goes.

Proof:

By doing the Taylor series expansion on equation (4.5), we have the following equation.

$$\begin{aligned} x_{1,n+1} &= x_{1,n} + \tau \cdot F_1\left(x_{1,n}, x_{2,n}\right) + O(\tau^2) \\ x_{2,n+1} &= x_{2,n} + \tau \cdot F_2\left(x_{1,n+1}, x_{2,n}\right) + O(\tau^2) \end{aligned} \tag{4.6}$$

Therefore, by neglecting the high order terms, we can have the following equation for the "explicit Euler method" approximation.

$$\begin{aligned} \bar{x}_{1,n+1} &= \bar{x}_{1,n} + \tau \cdot F_1\left(\bar{x}_{1,n}, \bar{x}_{2,n}\right) \\ \bar{x}_{2,n+1} &= \bar{x}_{2,n} + \tau \cdot F_2\left(\bar{x}_{1,n+1}, \bar{x}_{2,n}\right) \end{aligned} \tag{4.7}$$

Where $\bar{x}_{i,n}$ is the true states value, at time t_n, of the differential equation (4.6) that has been approximated by explicit Euler method. Then, the perturbed switching computational process for equation (4.7) can be written as follows as to obtain the solutions as close to $\bar{x}_{i,n}$ as possible,

$$\begin{aligned} \hat{x}_{1,n+1} &= \hat{x}_{1,n} + \tau \cdot F_1\left(\hat{x}_{1,n}, \hat{x}_{2,n}\right) + \tau \cdot \delta_{1,n} \\ \hat{x}_{2,n+1} &= \hat{x}_{2,n} + \tau \cdot F_2\left(\hat{x}_{1,n+1}, \hat{x}_{2,n}\right) + \tau \cdot \delta_{2,n} \end{aligned} \tag{4.8}$$

where $\delta_{i,n}$ represents the perturbations during computation, and which mainly comes from the round-off error at time $t = t_n$, $\hat{x}_{i,n}$ is the estimated value of $\bar{x}_{i,n}$ at time $t = t_n$ by switching computation scheme. Subtracting (4.7) from (4.8), we have the following,

$$\begin{aligned} \varepsilon_{1,n+1} &= \varepsilon_{1,n} + \tau \cdot [F_1\left(\hat{x}_{1,n}, \hat{x}_{2,n}\right) - F_1\left(\bar{x}_{1,n}, \bar{x}_{2,n}\right)] + \tau \cdot \delta_{1,n} \\ \varepsilon_{2,n+1} &= \varepsilon_{2,n} + \tau \cdot [F_2\left(\hat{x}_{1,n+1}, \hat{x}_{2,n}\right) - F_2\left(\bar{x}_{1,n+1}, \bar{x}_{2,n}\right)] + \tau \cdot \delta_{2,n} \end{aligned} \tag{4.9}$$

where the error (ε_i) is defined as the difference between the estimated state ($\hat{x}_i$) and the state ($\bar{x}_i$). By assuming F_1 is continuous at ($\bar{x}_1$, $\hat{x}_1$), according to the mean value theorem, we can have the following results for $a, b \in (0,1)$.

$$\begin{aligned} & F_1\left(\hat{x}_{1,n}, \hat{x}_{2,n}\right) - F_1\left(\bar{x}_{1,n}, \bar{x}_{2,n}\right) \\ &= F_1\left(\hat{x}_{1,n}, \hat{x}_{2,n}\right) - F_1\left(\bar{x}_{1,n}, \hat{x}_{2,n}\right) + F_1\left(\bar{x}_{1,n}, \hat{x}_{2,n}\right) - F_1\left(\bar{x}_{1,n}, \bar{x}_{2,n}\right) \\ &= \frac{\partial}{\partial x_1} F_1\left(a \cdot \hat{x}_{1,n} + (1-a) \cdot \bar{x}_{1,n}, \hat{x}_{2,n}\right) \cdot \varepsilon_{1,n} + \frac{\partial}{\partial x_2} F_1\left(\bar{x}_{1,n}, b \cdot \hat{x}_{2,n} + (1-b) \cdot \bar{x}_{2,n}\right) \cdot \varepsilon_{2,n} \end{aligned} \tag{4.10}$$

Therefore, by substituting (4.10) into (4.9), the error $\varepsilon_{1,n+1}$ can be rewritten as follows,

$$\varepsilon_{1,n+1} = \varepsilon_{1,n} + \tau \cdot [A_{1,x1,n} \cdot \varepsilon_{1,n} + A_{1,x2,n} \cdot \varepsilon_{2,n}] + \tau \cdot \delta_{1,n} \tag{4.11}$$

$$A_{1,x1,n} = \frac{\partial}{\partial x_1} F_1\left(a \cdot \hat{x}_{1,n} + (1-a) \cdot \bar{x}_{1,n},\ \hat{x}_{2,n}\right)$$

$$A_{1,x2,n} = \frac{\partial}{\partial x_2} F_1\left(\bar{x}_{1,n},\ b \cdot \hat{x}_{2,n} + (1-b) \cdot \bar{x}_{2,n}\right)$$

Similarly, we can write down the equations for $\varepsilon_{2,n+1}$,

$$\varepsilon_{2,n+1} = \varepsilon_{2,n} + \tau \cdot [A_{2,x1,n} \cdot \varepsilon_{1,n+1} + A_{2,x2,n} \cdot \varepsilon_{2,n}] + \tau \cdot \delta_{2,n} \tag{4.12}$$

$$A_{2,x1,n} = \frac{\partial}{\partial x_1} F_2\left(c \cdot \hat{x}_{1,n+1} + (1-c) \cdot \bar{x}_{1,n+1},\ \hat{x}_{2,n}\right)$$

$$A_{1,x2,n} = \frac{\partial}{\partial x_2} F_1\left(\bar{x}_{1,n+1},\ d \cdot \hat{x}_{2,n} + (1-d) \cdot \bar{x}_{2,n}\right)$$

Again, F_2 should be continuous at $(\bar{x}_2,\ \hat{x}_2)$ and $c, d \in (0,1)$.

Now, we want to eliminate $\varepsilon_{1,n+1}$ in the (4.12) by equation (4.11),

$$\varepsilon_{2,n+1} = \tau \cdot A_{2,x1,n} \cdot \varepsilon_{1,n} + (1 + \tau \cdot A_{2,x2,n}) \cdot \varepsilon_{2,n} + \tau \cdot \delta_{2,n} + O(\tau^2) \tag{4.13}$$

Again, neglecting the high order terms of time step, we can rearrange (4.11) and (4.13) into a matrix form.

$$E_{n+1} = A_n \cdot E_n + \tau \cdot D_n \tag{4.14}$$

$$E_n = \left[\varepsilon_{1,n}, \varepsilon_{2,n}\right]^T$$

$$A_n = \begin{bmatrix} 1 + \tau \cdot A_{1,x1,n} & \tau \cdot A_{1,x2,n} \\ \tau \cdot A_{2,x1,n} & 1 + \tau \cdot A_{2,x2,n} \end{bmatrix}$$

$$D_n = \left[\delta_{1,n}, \delta_{2,n}\right]^T$$

To find out the bound for the stability, the following matrix norm is introduced here.

$$\left\|E_{n+1}\right\| = \left\|A_n \cdot E_n + \tau \cdot D_n\right\| \tag{4.15}$$

Therefore, from Cauchy-Schwarz inequality, the local error bound with perturbations can be derived from (4.15),

$$\begin{aligned}\|E_{n+1}\| &= \|A_n \cdot E_n + \tau \cdot D_n\| \\ &\le \|A_n \cdot E_n\| + \|\tau \cdot D_n\| = \|A_n \cdot E_n\| + \tau \cdot \|D_n\| \\ &\le \|A_n\| \cdot \|E_n\| + \tau \cdot \|D_n\| \\ &\le \|A_n\| \cdot \|E_n\| + \tau \cdot D\end{aligned} \tag{4.16}$$

where D is the maximum bound of perturbations, and $\|D_n\| \le D$. Because the perturbation (δ) has noting to do with the error (E_n) propagation, we can find out a proper switching time step (τ) to facilitate $\|A_n\|_2 < 1$. Therefore, the switching computation scheme can be stable. □

The proof shown above only reveals the stability of this switching computation scheme, but not the convergence properties [14]. That is to say, the proof so far only guarantees that the error between switching computation value and discrete time system, shown in equation (4.6), does not grow. However, it does not say how accurate the estimated states $\hat{x}_{i,n}$ can be close to $\bar{x}_{i,n}$, let along $x_{i,n}$, which is the exact states value of the differential equation. It is obvious that for $\hat{x}_{i,n}$ to be close to $x_{i,n}$, the solution obtained from numerical approximation method ($\bar{x}_{i,n}$) must be close to $x_{i,n}$. and as accurate as possible. For that reason, we use "Runge-Kutta mthod" to approximate a continuous-time differential equation. The related stability issues are discussed in the following section.

4.2.4 Stability Analysis for "Runge-Kutta Method" Approximation

In this section, we provide the stability analysis of the switching scheme based on the Runge-Kutta method, which is adopted for the vehicle rollover simulations in this thesis. As shown in previous research that a high order Runge-Kutta method can guarantee the convergence of a nonlinear differential equation, we then assume no discretization error for the following proof work.

Proof:

By assuming the solution obtained by the Runge-Kutta method can be arbitrary close to the integral operation, the switching computational process can be written as follows,

$$\begin{aligned}\hat{x}_{1,n+1} &= \hat{x}_{1,n} + \int_{t_n}^{t_{n+1}} F_1\left(x_1(t), \hat{x}_{2,n}\right) dt \\ \hat{x}_{2,n+1} &= \hat{x}_{2,n} + \int_{t_n}^{t_{n+1}} F_2\left(\hat{x}_{1,n+1}, x_2(t)\right) dt\end{aligned} \tag{4.17}$$

As different from previous, the $\hat{x}_{i,n}$ means the estimated value of $x_{i,n}$ at time $t = t_n$ with perturbations. In the above equation, we can see that when one state is active, the other state is inactive, and *vice verse*. Then, subtracting (4.5) from (4.17),

$$\begin{aligned}\varepsilon_{1,n+1} &= \varepsilon_{1,n} + \int_{t_n}^{t_{n+1}} F_1\left(x_1(t), \hat{x}_{2,n}\right) dt - \int_{t_n}^{t_{n+1}} F_1\left(x_1(t), x_2(t)\right) dt \\ \varepsilon_{2,n+1} &= \varepsilon_{2,n} + \int_{t_n}^{t_{n+1}} F_2\left(\hat{x}_{1,n+1}, x_2(t)\right) dt - \int_{t_n}^{t_{n+1}} F_2\left(x_1(t), x_2(t)\right) dt\end{aligned} \tag{4.18}$$

where the error (ε_i) is defined the difference between the estimated state ($\hat{x}_i$) and the exact state (x_i).The last two terms of equation (4.18) can be processed as follow,

$$\begin{aligned}&\int_{t_n}^{t_{n+1}} F_1\left(x_1(t), \hat{x}_{2,n}\right) - F_1\left(x_1(t), x_2(t)\right) dt \\ &= \int_{t_n}^{t_{n+1}} F_1\left(x_1(t), \hat{x}_{2,n}\right) - F_1\left(x_1(t), x_{2,n}\right) + F_1\left(x_1(t), x_{2,n}\right) - F_1\left(x_1(t), x_2(t)\right) dt \\ &= \int_{t_n}^{t_{n+1}} F_1\left(x_1(t), \hat{x}_{2,n}\right) - F_1\left(x_1(t), x_{2,n}\right) dt + \int_{t_n}^{t_{n+1}} F_1\left(x_1(t), x_{2,n}\right) - F_1\left(x_1(t), x_2(t)\right) dt \\ &= \bar{\varepsilon}_{11,n} + \bar{\varepsilon}_{12,n}\end{aligned} \tag{4.19}$$

$$\bar{\varepsilon}_{11,n} = \int_{t_n}^{t_{n+1}} F_1\left(x_1(t), \hat{x}_{2,n}\right) - F_1\left(x_1(t), x_{2,n}\right) dt$$

$$\bar{\varepsilon}_{12,n} = \int_{t_n}^{t_{n+1}} F_1\left(x_1(t), x_{2,n}\right) - F_1\left(x_1(t), x_2(t)\right) dt$$

where $\bar{\varepsilon}_{1(i),n}$ represents the intermediate states error during the switching scheme, for $i = 1 \sim 2$. From the dynamics viewpoint, $\bar{\varepsilon}_{11,n}$ represents the convergent rate for the states error, and $\bar{\varepsilon}_{12,n}$ represents for the computation accuracy or perturbations. Therefore, we can separate errors into two terms, which represent $\bar{\varepsilon}_{11,n}$ and $\bar{\varepsilon}_{12,n}$ in (4.19), and discuss, respectively.

Firstly, using the mean value theorem, we can obtain more information of the error ($\bar{\varepsilon}_{11,n}$).

$$\begin{aligned}\bar{\varepsilon}_{11,n} &= \int_{t_n}^{t_{n+1}} F_1\left(x_1(t),\, \hat{x}_{2,n}\right) - F_1\left(x_1(t),\, x_{2,n}\right) dt \\ &= \int_{t_n}^{t_{n+1}} \frac{\partial}{\partial x_2} F_1\left(x_1(t),\, \mathrm{e}\right) \cdot \varepsilon_{2,n}\; dt \\ &= \varepsilon_{2,n} \cdot \int_{t_n}^{t_{n+1}} \frac{\partial}{\partial x_2} F_1\left(x_1(t),\, \mathrm{e}\right) dt\end{aligned} \tag{4.20}$$

where F_1 is continuous at ($x_{2,n}$, $\hat{x}_{2,n}$) and $\mathrm{e} \in (0,1)$. Furthermore, with assuming the Runge-Kutta method can obtain the numerical solution close to the exact solution of above equations, and linear respect to the time step (τ), we can rewrite (4.20) as follows,

$$\begin{aligned}\bar{\varepsilon}_{11,n} &= \varepsilon_{2,n} \cdot \int_{t_n}^{t_{n+1}} \frac{\partial}{\partial x_2} F_1\left(x_1(t),\, e\right) dt \\ &= \varepsilon_{2,n} \cdot \tau G_1(x_1, x_2)\end{aligned} \tag{4.21}$$

where G_1 represents the exact solution of the integral operation shown above, which is obtained by the Runge-Kutta method.

Secondly, for obtaining the expansion of the error ($\bar{\varepsilon}_{12,n}$), we let the upper bound (t_{n+1}) to be a variable (σ), and we can rewrite the error ($\bar{\varepsilon}_{12,n}$) as follows:

$$\bar{\varepsilon}_{12,n} = \int_{t_n}^{\sigma} F_1\left(x_1(t),\, x_{2,n}\right) - F_1\left(x_1(t),\, x_2(t)\right) dt \tag{4.22}$$

Using the Taylor expansion around $\sigma = t_n$, we can expand the error ($\bar{\varepsilon}_{12,n}$) as follows,

$$\begin{aligned}\bar{\varepsilon}_{12,n} &= \int_{t_n}^{\sigma} F_1\left(x_1(t),\, x_{2,n}\right) - F_1\left(x_1(t),\, x_2(t)\right) dt \\ &= 0 + (\sigma - t_n) \cdot \left[F_1\left(x_1(\sigma),\, x_{2,n}\right) - F_1\left(x_1(\sigma),\, x_2(\sigma)\right)\right] \frac{\partial \sigma}{\partial \sigma} \\ &\quad + \frac{1}{2}(\sigma - t_n)^2 \cdot \left\{ \begin{array}{l} \dfrac{\partial x_2}{\partial \sigma}\left[\dfrac{\partial}{\partial x_2} F_1\left(x_1(\sigma),\, x_{2,n}\right) - \dfrac{\partial}{\partial x_2} F_1\left(x_1(\sigma),\, x_2(\sigma)\right)\right] \\ + \dfrac{\partial x_1}{\partial \sigma}\left[\dfrac{\partial}{\partial x_1} F_1\left(x_1(\sigma),\, x_{2,n}\right) - \dfrac{\partial}{\partial x_1} F_1\left(x_1(\sigma),\, x_2(\sigma)\right)\right] \end{array} \right\} \\ &\quad + O((\sigma - t_n)^3)\end{aligned} \tag{4.23}$$

Then, we set the upper bound is t_{n+1} to obtain the result of the error ($\bar{\varepsilon}_{12,n}$).

$$\begin{aligned}\bar{\varepsilon}_{12,n} &= \tau \cdot \left[F_1\left(x_{1,n+1}, x_{2,n}\right) - F_1\left(x_{1,n+1}, x_{2,n+1}\right)\right] \\ &\quad -\frac{1}{2}\tau^2 \cdot \dot{x}_2 \cdot \frac{\partial}{\partial x_2} F_1\left(x_1(\sigma), x_2(\sigma)\right)\Big|_{\sigma=t_{1,n+1}} \\ &\quad + O(\tau^3)\end{aligned} \tag{4.24}$$

Therefore, incorporating equations (4.21) and (4.24) into equations (4.18) and (4.19), the error ($\varepsilon_{1,n+1}$) can be rearranged as follows,

$$\begin{aligned}\varepsilon_{1,n+1} &= \varepsilon_{1,n} + \bar{\varepsilon}_{11,n} + \bar{\varepsilon}_{12,n} \\ \bar{\varepsilon}_{11,n} &= \varepsilon_{2,n} \cdot \tau G_1(x_1, x_2) \\ \bar{\varepsilon}_{12,n} &= \tau \cdot \left[F_1\left(x_{1,n+1}, x_{2,n}\right) - F_1\left(x_{1,n+1}, x_{2,n+1}\right)\right] \\ &\quad -\frac{1}{2}\tau^2 \cdot \dot{x}_2 \cdot \frac{\partial}{\partial x_2} F_1\left(x_1(\sigma), x_2(\sigma)\right)\Big|_{\sigma=t_{1,n+1}} \\ &\quad + O(\tau^3)\end{aligned} \tag{4.25}$$

In the same way, we can also express the error ($\varepsilon_{2,n+1}$) as follows,

$$\begin{aligned}\varepsilon_{2,n+1} &= \varepsilon_{2,n} + \bar{\varepsilon}_{21,n} + \bar{\varepsilon}_{22,n} \\ \bar{\varepsilon}_{21,n} &= \varepsilon_{1,n+1} \cdot \int_{t_n}^{t_{n+1}} \frac{\partial}{\partial x_1} F_2\left(\mathrm{f}, x_2(t)\right) dt = \varepsilon_{1,n+1} \cdot \tau G_2(x_1, x_2) \\ \bar{\varepsilon}_{22,n} &= -\frac{1}{2}\tau^2 \cdot \dot{x}_1 \cdot \frac{\partial}{\partial x_1} F_2\left(x_1(\sigma), x_2(\sigma)\right)\Big|_{\sigma=t_{1,n+1}} \\ &\quad + O(\tau^3)\end{aligned} \tag{4.26}$$

Again, F_2 should be continuous at ($x_{1,n+1}$, $\hat{x}_{1,n+1}$) and $\mathrm{f} \in (0,1)$. G_2 represents the exact solution of the integral operation shown above, and is obtained by the Runge-Kutta method.

Furthermore, because ε_1 and ε_2 have no common state, we can rearrange (4.25) and (4.26) as the matrix form, and obtain the matrix norm to find out the bound of the stability.

$$\left\|E_{n+1}\right\| = \left\|A_n \cdot E_n + \bar{E}_n\right\| \tag{4.27}$$

where $E_n = \left[\varepsilon_{1,n}, \varepsilon_{2,n}\right]^T$

$$A_n = \begin{bmatrix} 1 & \tau G_1 \\ \tau G_2 & 1 + \tau^2 G_1 G_2 \end{bmatrix}$$

$$\bar{E}_n = \left[\bar{\varepsilon}_{12,n}, \tau G_2 \bar{\varepsilon}_{12,n} + \bar{\varepsilon}_{22,n}\right]^T$$

From Cauchy-Schwarz inequality, the global error bound with perturbations can be derived from (4.26),

$$\begin{aligned} \|E_{n+1}\| &= \|A_n \cdot E_n + \overline{E}_n\| \\ &\le \|A_n\| \cdot \|E_n\| + \|\overline{E}_n\| \\ &\le \|A_n\| \cdot \|E_n\| + \gamma(\tau) \end{aligned} \tag{4.28}$$

where $\gamma(\tau)$ represents the maximum bound of $\|\overline{E}_n\|$. Additionally, because $\|\overline{E}_n\|$ is a function of time step (τ), we can assume the bound is also a function of time step. However, the bound ($\gamma(\tau)$) has nothing to do with the states error convergence. Therefore, we can choose a proper switching time step (τ) to achieve $\|A_n\|_2 < 1$, and thus the system can be guaranteed to be stable. □

In this section, the analysis work indicate that, by assuming the exact solution of a continuous-time differential equation can be obtained by the Runge-Kutta method, we can can find a proper switching time (τ) to guarantee the stability for this switching computation scheme. Furthermore, by assuming $F_1(x_{1,n+1}, x_{2,n}) \cong F_1(x_{1,n+1}, x_{2,n+1})$ for a stable system, this switching scheme based on the Runge-Kutta method can precisely estimate the states with the error of $O(\tau^2)$.

4.3 Sensor Selections

In this section, suitable sensors are chosen for the observer construction. According to the information obtained by various sensors, the determination of sensors depends on the states convergence. Although, in this thesis, we are unable to develop an organized methodology to discover the optimal sensor and optimal location effectively, we can guarantee this set of sensors, which is chosen in this section, will achieve the destination in states convergence.

x	0	0	1	0	0	0	0	0
$\dot{x}$	3.99e-7	0	0	0.1893	-0.9751	0.0705	-0.0120	0.09131
y	0	-1	0	0	0	0	0	0
$\dot{y}$	-4.06e-8	0	0	-0.0193	0.1018	0.1840	-0.1653	0.9634
ε	-1	0	0	2.05e-6	-1.06e-8	2.2e-16	-1.0e-21	6.1e-26
$\dot{\varepsilon}$	-7.19e-9	0	0	-0.0034	0.0176	0.3990	-0.8873	-0.2304
ω_1	-1.51e-8	0	0	-0.0071	0.0485	0.8955	0.4303	-0.1025
ω_2	-2.02e-6	0	0	-0.9817	-0.1904	0.0021	0.0009	0.0003

Table 4.1 The eigenvector of the observability grammian when the output is lateral acceleration

-8.4e-20	0	0	0	0	0	0	0
0	0	0	0	0	0	0	0
0	0	0	0	0	0	0	0
0	0	0	1.2e-15	0	0	0	0
0	0	0	0	1.0e-12	0	0	0
0	0	0	0	0	0.0005	0	0
0	0	0	0	0	0	0.3369	0
0	0	0	0	0	0	0	13.145

Table 4.2 The eigenvalue of the observability grammian when the output is lateral acceleration

4.3.1 Sensors for Yaw Model

The main objective of the yaw model observer is to provide accurate lateral acceleration information since the lateral acceleration is the input to the roll model. However, the lateral acceleration can not be accurately predicted without all its associated states converging to their correct values. In order to reveal which states are strongly associated with the lateral acceleration and what sensors should be incorporated to enable states convergence, we construct the observability grammian from the linearized yaw model.

Table 4.1 and Table 4.2 show the eigenvectors and eigenvalues of the observability grammian when the lateral acceleration is set for the system output. The eigenvalues chart indicates that only three modes are strongly related to the lateral acceleration. The eigenvector chart indicates that these three modes consist of yaw rate, lateral velocity, front wheel angular rate and a small portion of longitudinal velocity. Since 3 modes but 4 states are crucial to the

estimation of lateral acceleration, we may need one more sensor, other than the lateral acceleration sensor, to ensure all these 4 states converging to their correct values. To this mean, the observability grammian is constructed again for the system output being longitudinal velocity. Table 4.3 and Table 4.4 show the eigenvectors and eigenvalues of this observability grammian.

x	1	0	0	0	0	0	0	0
$\dot{x}$	0	0	2.6e-17	6.45e-8	-1.19e-5	0.0012	0.0101	0.9999
y	0	1	0	0	0	0	0	0
$\dot{y}$	0	0	-2.1e-10	-0.5743	-0.2506	0.7592	0.1761	-0.0027
ε	0	0	-1	3.6e-10	-1.8e-13	1.0e-16	-3.9e-20	-1.4e-31
$\dot{\varepsilon}$	0	0	-5.1e-11	-0.1402	-0.1002	-0.3526	0.9198	-0.0088
ω_1	0	0	-2.9e-10	-0.8002	0.31242	-0.4425	-0.2575	0.0031
ω_2	0	0	-3.7e-11	-0.1010	-0.9108	-0.3219	-0.2380	0.0028

Table 4.3 The eigenvector of the observability grammian when the output is longitudinal velocity

0	0	0	0	0	0	0	0
0	0	0	0	0	0	0	0
0	0	2.1e-22	0	0	0	0	0
0	0	0	1.1e-13	0	0	0	0
0	0	0	0	9.7e-10	0	0	0
0	0	0	0	0	4.6e-6	0	0
0	0	0	0	0	0	0.00028	0
0	0	0	0	0	0	0	7.9951

Table 4.4 The eigenvalue of the observability grammian when the output is longitudinal velocity

As shown in the eigenvalues and eigenvectors chart, the longitudinal velocity is not strongly related to any other states. Therefore, we choose longitudinal velocity sensor as the second sensor for the yaw model.

As shown in the above description, we choose two sensors, which can measure the physical quantity of the lateral acceleration and longitudinal velocity respectively, to work with the observer. And this observer, which will be discussed later, is based on the vehicle yaw model.

4.3.2 Sensors for Roll Model

Most of the research works utilized inertial roll rate sensor and/or roll angle sensor to sense the vehicle roll angle. However, the information obtained from these two sensors is coupled with the vehicle roll angle and the road bank angle [20]. The vehicle rollover incidence is declared by the vehicle roll angle relative the road level. Therefore, the inertial sensors mentioned above are not feasible. In other words, the eligible sensor for this application must be capable of detecting vehicle roll angle in the “road frame”, instead of “global frame”.

For the above-mentioned reason, we choose suspension displacement sensor for the roll model. The advantage of that is this physical quantity of four suspensions is unable to couple with road angles, such as bank angle and tilt angle shown in figure 2.8. In the other words, the deflection of the suspension is only induced by the vehicle roll motion (ϕ), the vehicle pitch motion (θ) and the vehicle vertical motion (z), as shown in equation 2.30. Additionally, the observability matrix of the linearized roll model is full rank. Therefore, the suspension displacement corresponds to our destination of the sensor determination.

As shown in the above description, we choose one sensor, which can measure the physical quantity of the suspension displacement, to work with the observer. And this observer, which will be discussed later, is based on the vehicle roll model.

4.4 Nonlinear Observer Algorithm

The first order extended Kalman filter (EKF) is chosen to be the observer algorithm mainly because it can work with nonlinear systems (yaw, roll models) and it is effective in the noise reduction when the measurements are contaminated by noise. EKF has been questioned for the capability of states convergence [3] [8]. In that case, we can use Iterative Kalman Filter algorithm to work out both noise reduction and states convergence.

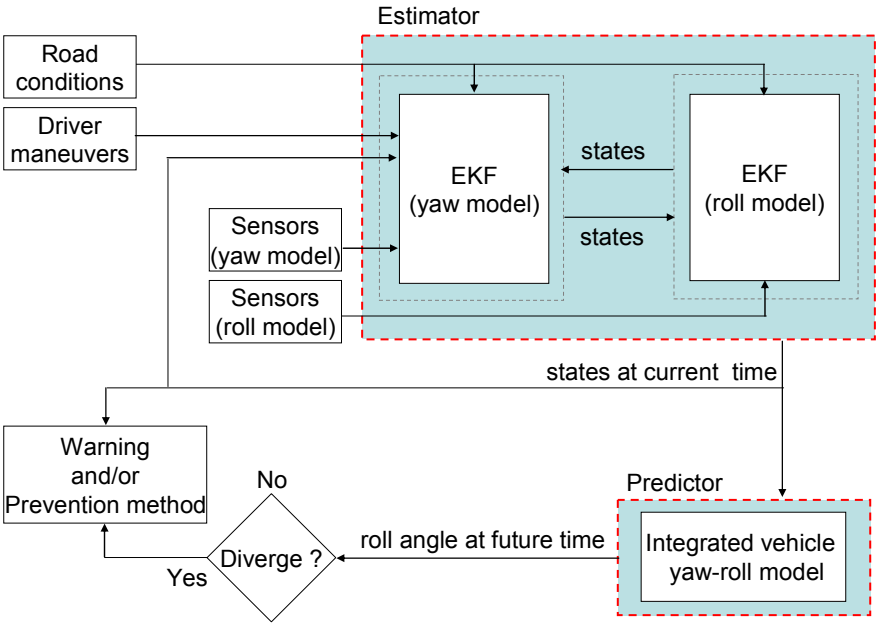

Figure 4.4 Block diagram of the vehicle rollover prediction system

4.5 Block Diagram for the Prediction System

Figure 4.4 shows the block diagram of the proposed vehicle rollover prediction system. As shown in the diagram, the driver maneuver, such as steering, braking, tracking and etc are fed into estimator as the system inputs. The estimator produces vehicle states information in real-time with information from system inputs and sensor outputs. These states real-time information is then fed into predictor to obtain the vehicle roll angle in future time. A rollover incidence is declared based on the rollover angle in future time.

Chapter 5
Simulation and Results

The following simulations are meant to elucidate the feasibility of the proposed rollover prediction method. In these simulations, the vehicle is moving at the longitudinal speed of 90 km/hr and making a quick turn at the 4th second. The simulation includes five situations and each differs from the steering wheel maneuvering and/or vehicle on a slanted road. The simulation results are shown in figure 5.1~5.6 and the plot is arranged in the following order: steering wheel angle in the upper left, lateral acceleration in the lower left, roll angle in upper the middle, roll rate in lower the middle, yaw angle in the upper right and yaw rate in the lower right. Furthermore, the yaw-roll model outputs are drawn in solid-blue lines while the predictor output is drawn in dash-green lines. The vehicle parameters utilized in simulations are listed in Appendix B.

For the comparison purpose, the output of the predictor is intentionally set to obtain current states information, instead of states information in future time. Furthermore, three sensors (lateral acceleration sensor, longitudinal velocity sensor and suspension displacement sensors) are turned on between 0~5 second and then turned off to the end of the simulation. Also, during 5~8 second, the steering wheel angle is kept at the same. With the above arrangements, the simulation results shown in solid-blue lines can be treated as the real vehicle response; the green-dash lines can be treated as the estimator output for the timeline within 0~5 second and as the predictor output for the timeline after the 5th second.

In the reminder of this section, we will verify the vehicle rollover prediction system by the real vehicle, which is the integrated yaw-roll model as shown in chapter 3. On one hand, the convergence of the observer-based estimator will be checked between 0~5 second. On the other hand, the accuracy of the model-based predictor will be checked between 5~10 second. Additionally, keeping the same driving maneuver during 5~8 second looks like the future dynamic behavior at the 5th second. And, changing the driving maneuver after the 8th second will check the inactivity of sensors. Lastly, we will declare the vehicle rollover by the vehicle roll angle in the future time.

5.1 Case I

Case I shows a vehicle doing a smooth turn on a flat road. As shown in figure 5.1, the estimator observes the vehicle roll motion very well and the predictor successfully predicts the vehicle roll motion. There is an obvious deviation between vehicle response and predictor output after 8^{th} second. That is because the steering wheel angle changes again at 8^{th} second and this command input, as expected, is not aware of by the predictor. Furthermore, both estimator and predictor do not work well for the vehicle yaw angle.

5.2 Case II

Case II shows a vehicle doing a quick turn on a flat road. As shown in figure 5.2, the vehicle roll angle diverge and a rollover happening. Again, the estimator can observe the vehicle roll motion very well and the predictor can successfully predict the vehicle rollover. In addition, the estimation of vehicle yaw angle still does not follow the vehicle yaw angle.

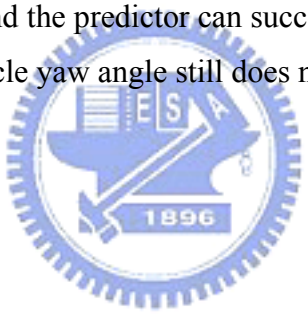

5.3 Case III

Case III shows a vehicle doing a slow turn on a slanted road with the slop of -25 degrees from the horizontal. As shown in figure 5.3, the vehicle rollover and the prediction system successfully predict this situation. The only difference between simulation conditions in Case I and Case III is the road bank angle.

This example demonstrates how the road bank angle can initiate a rollover incidence. Additionally, the estimator successfully observes the vehicle yaw angle in this case but not the other. This is because the lateral acceleration is affected by the yaw angle when the vehicle is on a slope and thus the yaw angle being observed through lateral acceleration sensor.

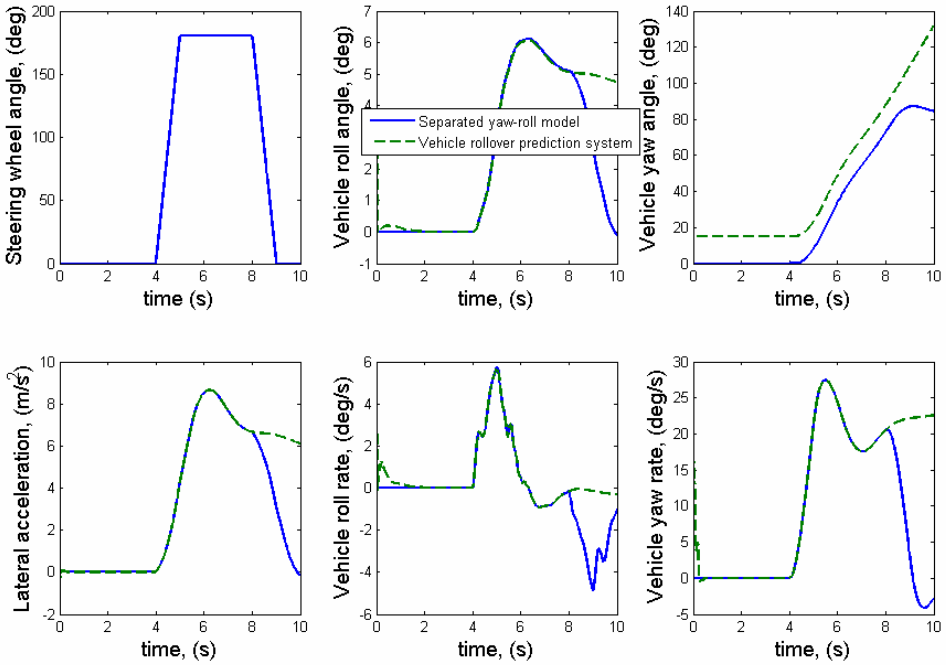

Figure 5.1 Comparison of vehicle response and rollover prediction system output in Case I, in which the vehicle does not rollover.

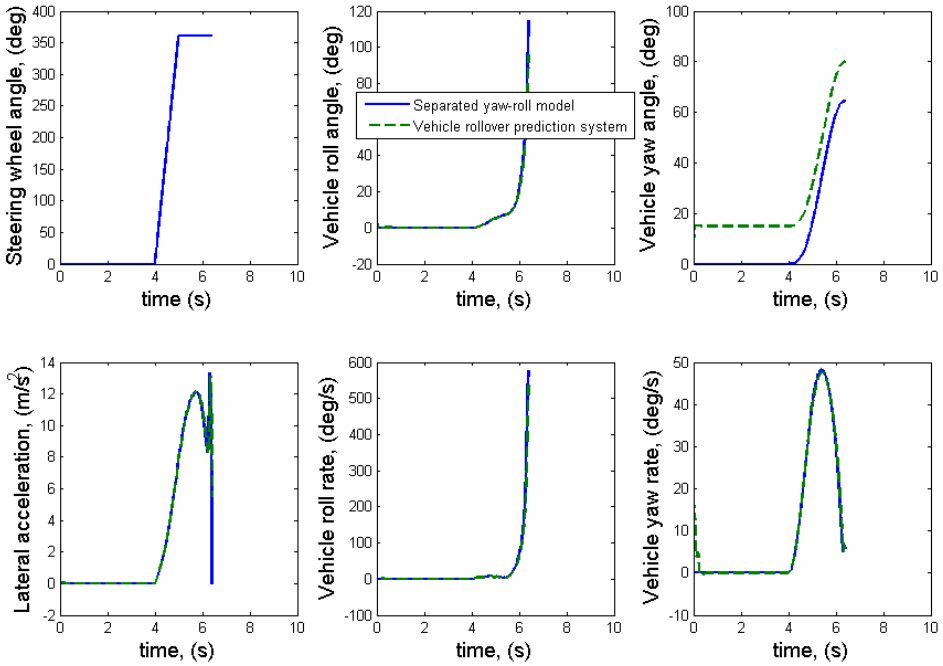

Figure 5.2 Comparison of vehicle response and rollover prediction system output in Case II, in which the vehicle rollover.

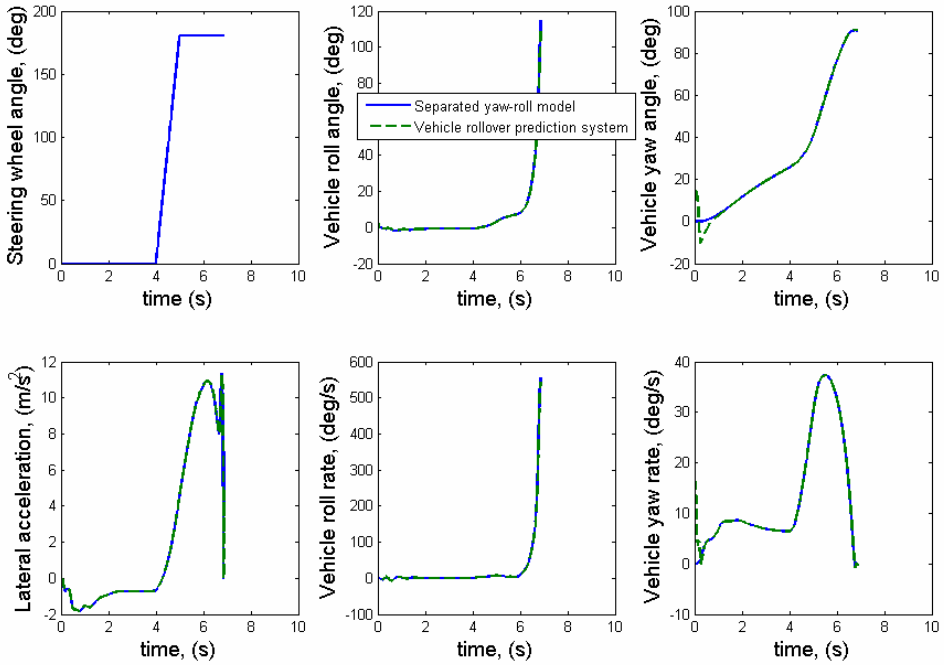

Figure 5.3 Comparison of vehicle response and rollover prediction system output in Case III, in which the vehicle rollover due to road bank angle.

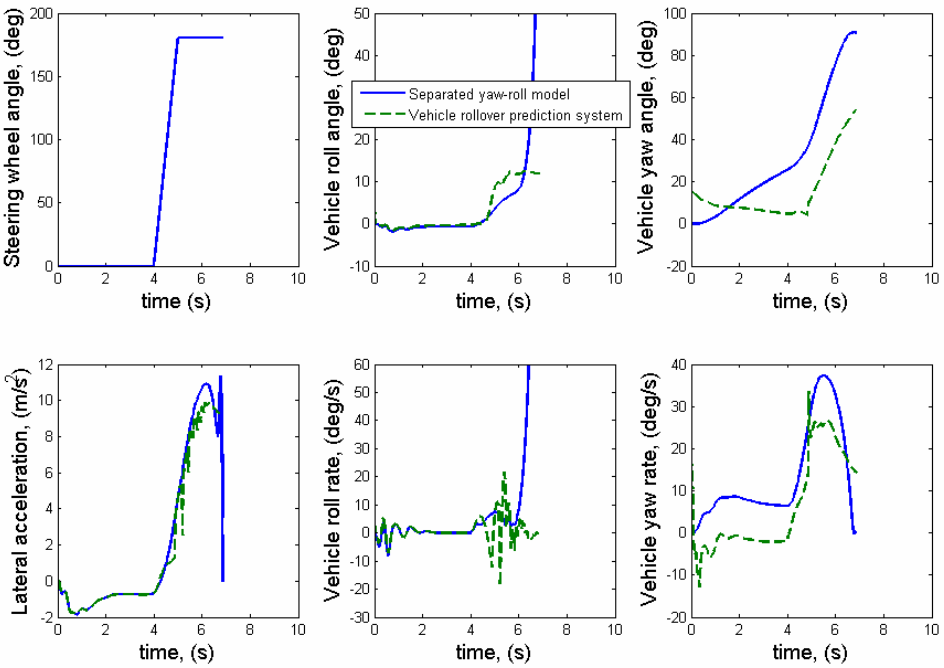

Figure 5.4 Comparison of vehicle response and rollover prediction system output in Case IV, in which the vehicle rollover but the prediction failed, due to neglecting the road bank condition.

5.4 Case IV

Case IV shows a vehicle doing a slow turn on a slanted road with the slop of -25 degrees from the horizontal, while the prediction system exclude the road bank condition in the modeling. As shown in figure 5.4, the prediction system can neither estimate the states nor predict the states correctly.

Case IV and Case III are mean to demonstrate the importance of incorporating the road bank condition in the vehicle model.

5.5 Case V

Case V shows a vehicle doing a smooth turn on a flat road. The simulation condition is the same as in Case I, except the car response (solid-blue lines) are obtained from the full-car model. As shown in figure 5.5, the prediction system, which based on the yaw-roll model, failed to estimate the system states.

The deviation shown in figure 5.5 obviously came from the difference between full-car model and yaw-roll model. To identify which step in the model simplification process results in this big deviation, we compare the vehicle response obtained from full-car model, separated yaw-roll model and separated yaw-roll model with pitch motion. As shown in figure 5.6, the response of yaw-roll model with pitch motion is very close to the response of full car model, except at some high frequency content.

This simulation results suggest that, when focused on the vehicle roll dynamics, broken down the full-car model into several subsystems is feasible. However, neglecting the Euler pitch motion may be erroneous.

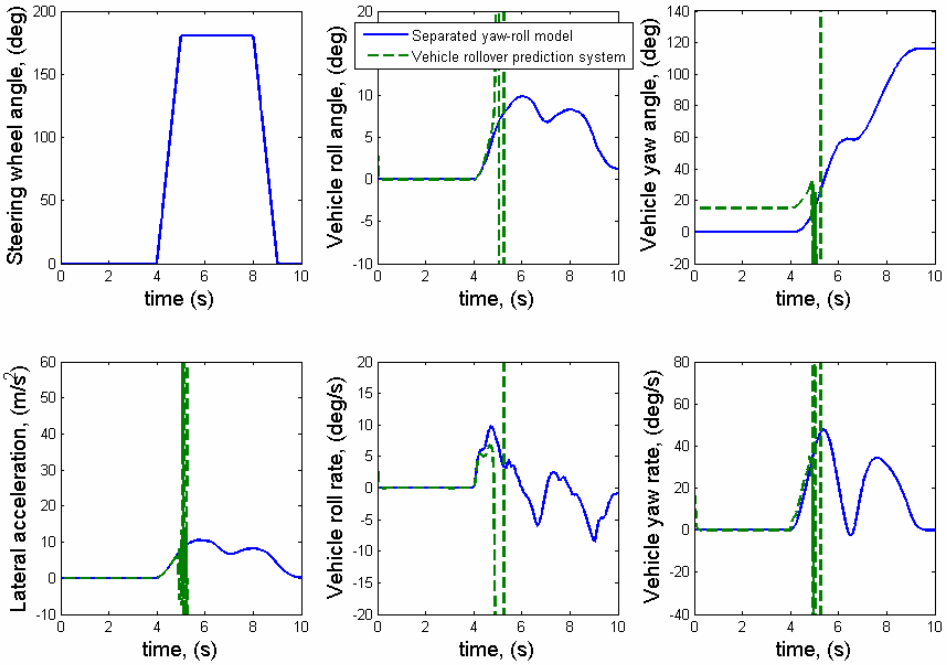

Figure 5.5 Comparison of vehicle response and rollover prediction system output in Case V.

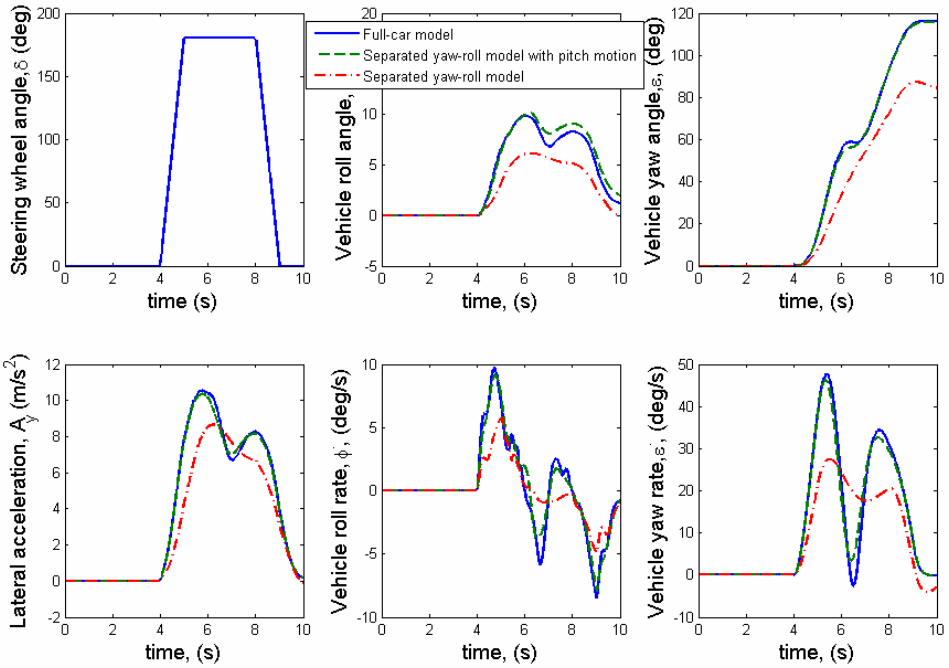

Figure 5.6 Comparison between full-car model, separated yaw-roll model with pitch motion and separated yaw-roll model.

5.6 Conclusions

A vehicle rollover prediction system proposed in this thesis achieves two goals: the estimation in real-time vehicle dynamics and the prediction in future vehicle dynamics. In these predicted vehicle states, we especially observe the vehicle roll angle in future time. With this physical quantity, we can declare the vehicle rollover in future time while keeping the same driving maneuver. Additionally, we can also take these predicted vehicle states to present the relative orientation of the vehicle in future time.

Simulation results indicated that road bank condition plays an important role in rollover incidences. This factor should be dealt with in two phases. Firstly, the road bank condition should be included in the vehicle model. Secondly, the selected sensor should be truly reflecting the vehicle roll angle relative to the road bank angle. These two challenges are solved by introducing the “road frame” into vehicle modeling and adopting suspension displacement sensors.

Simulation results also indicated that the Euler pitch motion has less effect on the vehicle roll angle estimation but may still result in intolerable deviation when it is neglected. More research work should be done in investigating the effect of neglecting vehicle pitch motion instead of Euler pitch motion for a better approximation to real driving situations. Furthermore, simulation results also suggest that a separated yaw-roll-pitch model could be a possible solution to this application.

Chapter 6

Conclusions and Future Works

6.1 Conclusions

In this thesis, we touched upon several topics for the vehicle rollover prediction system. The main contributions of this thesis include the full-car modeling, the novel observability matrix, the ADI-like method and its stability analysis, and the vehicle rollover prediction system. The work done in each topic is summarized as follows.

Full-car model

The proposed vehicle rollover prediction system is developed based on the vehicle full-car model, which is obtained from the vehicle physical features, performance, road conditions, etc, instead of a set of empirical parameters. Therefore, this prediction method can be easily tailored for various types of four-wheels vehicles and accommodate for different driving maneuvers. This approach presents a strong evidence for the vehicle rollover prediction.

A vehicle rollover is declared for the vehicle roll angle relative to the road. Therefore, the consideration of road condition in a rollover prediction system should be a must. Simulation results also indicated that a full-car model, incorporated with the road condition, can successfully predict a rollover event for the case that a car doing a quick turn on a slope, while a full-car model without road condition does not.

Novel observability matrix

The novel system observability matrix is developed to reveal the connection between vehicle roll motion and other vehicle dynamics. It provides firm evidence for the modeling reduction task. This approach, using covariance matrix to reveal the states relations, is

particularly suitable to a complicated nonlinear system with a wide operation range. However, more theoretical work should be done to investigate the reliability of this new observability matrix.

Switching scheme in the ADI-like method

A vehicle rollover prediction system based on the separated yaw-roll model is developed and verified by simulation results. The separated yaw-roll model, accompanied with switching computation scheme, enables the nonlinear observer design, which the observer design is almost impossible for the complicated full-car model. Furthermore, the stability analysis, as shown in chapter 4, indicates that the switching computation scheme can perform a stable computing by a proper choice of simulation time-step.

Vehicle rollover prediction system

A vehicle rollover prediction system proposed in this thesis is developed and verified by simulation results. The observer-based estimator, the first part of this prediction system, can obtain more states information in real-time by deploying limited amount of sensors. Additionally, the estimated vehicle states can be recorded in a so-called “Vehicle Black Box” for multiple vehicle applications. The model-based predictor, the second part of this prediction system, can predict vehicle states in future time by the integrated yaw-roll model. Additionally, the predicted vehicle states can be the evidence for declaring a vehicle rollover.

6.2 Future Works

In this thesis, some of the conceptual work for the proposed vehicle rollover prediction system is verified by simulation results. However, more mathematical work should be done for the reliability and optimization analysis. Some future works for this study are summarized in the following.

Full-state vehicle model with automotive engine

Simulation result indicates that the dynamic response of the full-car model is different from that of the separated yaw-roll model, but similar to the separated yaw-roll-pitch model. However, in this thesis, we take the separated yaw-roll model as an example for simple verification. In order to get close to the real situation, a vehicle rollover prediction system should adopt the separated yaw-roll-pitch model for the subsequent observer construction work.

Currently, the simulation wok does not include the engine and power-train system in the full-car modeling, and thus the driver has very limited control over the vehicle dynamics. The next step is to include more vehicle components, such as engine and power-train system, in the simulation work so that we can investigate more driver maneuvers during a rollover incidence.

Optimal sensor type and location

The sensor type and location, in this thesis, are chosen for the reasons shown in chapter 4. However, the choice of the sensor type and location is not optimal yet. The sensor choice could be determined by the observability covariance matrix [24]. Therefore, it is possible to combine a cost function with observability covariance matrix to achieve the optimal sensor location and selection for this prediction system.

Rollover prevention measures

This vehicle rollover prediction system proposed in this thesis can provide the vehicle states information for the subsequent rollover warning or prevention system. Since the information provided by this prediction technique is much richer than other approaches, we can design various prevention measures and determine which one to be in effect according to the rollover conditions. This approach can provide a safety measure for the driver while minimize the unnecessary interferences to the driver maneuvering.

Reference

[1] Acarman T. and Ozguner U., “Rollover prevention for heavy trucks using frequency shaped sliding mode control,” *Proceedings of IEEE Conference on Control Applications*, Vol. 1, pp. 7 – 12, 2003.

[2] Allen, R. W., Theodore J. R., David H. K. and Jeffrey P. C., "Vehicle and tire modeling for dynamic analysis and real-time simulation," *Society of Automotive Engineers Automotive Dynamics and Stability Conference*, SAE Paper No. 2000-01-1620, May 2000.

[3] Bar-Shalom Y. , Li X. R. and Kirubarajan T., Estimation with Applications to Tracking and Navigation, Wiley-Interscience, 2001.

[4] Chen B. and Peng H., "A real-time rollover threat index for Sports Utility Vehicles," *Proceedings of the American Control Conference*, pp. 1233-1237, June 1999.

[5] Chen C.-T., Linear System Theory and Design, Library of Congress Cataloging in Publication Data, 1984.

[6] Day T. D., “Validation of the EDVSM 3-dimentional vehicle simulator,” *Society of Automotive Engineers International Congress and Exposition*, SAE Paper No. 970958, February 1997.

[7] Feng K. T., “Vehicle lateral control for driver assistance and automated driving,” *Ph.D. Thesis*, Department of Mechanical Engineering, University of California, Berkeley, 2000.

[8] Grewal M. S. and Andrews A. P., Kalman Filtering : Theory and Practice Using Matlab, Wiley-Interscience, 2001.

[9] Grzywna J. W., Ivano N. M., Schwartz E. M. and Arroyo A. A., “KELVIN: A second generation land vehicle,” *Proceedings of the Conference on Recent Advances in Robotics*, May 2002.

[10] Hac A., Brown T. D. and Martens J. D., “Detection of vehicle rollover,” *Proceedings of the SAE World Congress and Exhibition*, SAE Paper No. 2004-01-1757, March 2004.

[11] Hahn J. and Edgar T. F., “Nonlinearity quantification and model classification using gramians and other covariance matrices,” *Proceedings of the AIChE 2001 Annual Meeting*, Reno, 2001.

[12] Hauth M., “Numerical techniques for cloth simulation”, *Clothing Simulation and Animation*, in: ACM SIGGRAPH Course 29, 2003.

[13] Hingwe P., “Robustness and performance issues in the lateral control of vehicle in automated highway system,” *Ph. D. Thesis*, Department of Mechanical Engineering, University of California, Berkeley, 1997.

[14] Hundsdorfer W. H. and Verwer J. G., “Stability and convergence of the Peaceman-Rachford ADI method for initial-boundary value problems,” *Mathematics of Computation*, Vol. 53, Num. 187, pp. 81-101, July 1989.

[15] Pacejka H. B. and Besselink I. J. M., "Magic formula tyre model with transient properties," *Vehicle System Dynamics Supplement*, Vol. 27, pp. 234-249, 1997.

[16] Pacejka H. B. and Bakker E., "The magic formula tyre model," *Vehicle System Dynamics Supplement*, Vol. 21, pp. 1-18, 1993.

[17] Porcel, A., Laurence, P., Basset, M. and Gissinger, G. L., "Tyre model for vehicle simulation: Overview and real time solution for critical situations," *Proceedings of the IEEE International Conference on Control Applications*, pp. 817-822, September 2001.

[18] Rogers S. and Wenbing Z., "Development and evaluation of a curve rollover warning system for trucks," *Proceedings of IEEE on Intelligent Vehicles Symposium*, pp. 294 – 297, 2003.

[19] Ryu J. and Gerdes J. C., "Integrating inertial sensors with GPS for vehicle dynamics control," *ASME Journal of Dynamic Systems on Measurement and Control*, June 2004.

[20] Ryu J. and Gerdes J. C., "Estimation of vehicle roll and road bank angle," *Proceedings of the American Control Conference*, 2004.

[21] Sanchez E.N., Ricalde L.J., Langari R. and Shahmirzadi D., "Recurrent neural control for rollover prevention on heavy vehicles," *Proceedings of IEEE International Joint Conference on Neural Networks*, Vol. 3, pp. 1841-1846, July 2004.

[22] Scholpp G., Schmidt J., Hofmann R., Friberger M. and Wolf F., "Influences of parameters at vehicle rollover", *Proceedings of the International Body Engineering Conference and Exposition*, SAE. Paper No. 2000-01-2669, October 2000.

[23] Schubert P. J., Nichols D., Wallner E., Kong H. and Schiffmann J., "Electronics and algorithms for rollover sensing," *Proceedings of the SAE World Congress and Exhibition*, SAE Paper No. 2004-01-0343, March 2004.

[24] Singh A. K. and Hahn J., "Determining optimal sensor location for state and parameter estimation for stable nonlinear system," *Industrial an Engineering Chemical Research*, Vol. 44, pp. 5645-5659, 2005.

[25] Stetter H. J., Analysis of Discretization Methods for Ordinary Differential Equations, Springer-Verlag Berlin Heidelberg, New York, 1973.

[26] Takano S. and Nagai M., "Dynamics control of large vehicle for rollover prevention," *Proceedings of the IEEE International Vehicle Electronics Conference*, pp. 85-89, September 2001.

[27] Travis W. E., Whitehead R. J., Bevly D. M., and Flowers G. T., "Using scaled vehicles to investigate the influence of various properties on rollover propensity," *Proceedings of the American Control Conference*, pp. 3381-3386, 2004.

[28] Trent V. and Greene M., "A genetic algorithm predictor for vehicular rollover," *IECON02*, Vol. 3, pp. 1752-1756, 2002.

[29] Ungoren A. Y., Peng H. and Milot D., "Rollover propensity evaluation of an SUV equipped with a TRW VSC system," Society of Automotive Engineers Congress and *Exposition*, SAE Paper No. 2001-01-0128, 2001.

[30] Vidyasagar M., Nonlinear Systems Analysis, Prentice Hall, New Jersey, 1993.

[31] Whitehead R., Travis W., Bevly D. M., and Flowers G., “A study of the effect of various vehicle properties on rollover property,” *Proceedings of the Automotive Dynamics and Stability Conference and Exhibition*, SAE Paper No. 2004-01-2094, May 2004.

Appendix

A. The Separation of the Integrated Yaw-Roll Model from Euler Transformation

After neglecting the vehicle pitch motion, the governing equation of the rotational motion is shown in equation (3.1) by Euler transformation. The equations are rewritten as follows:

$$\begin{aligned}\ddot{\phi} &= \frac{M_x}{I_x} - \frac{I_z - I_y}{I_x}\left(\dot{\varepsilon}^2 \sin\phi\cos\phi\right) \\ \ddot{\varepsilon} &= \left(\frac{M_y}{I_y} - \frac{I_x - I_z}{I_y}\left(\dot{\phi}\dot{\varepsilon}\cos\phi\right)\right)\sin\phi + \left(\frac{M_z}{I_z} - \frac{I_y - I_x}{I_z}\left(\dot{\phi}\dot{\varepsilon}\sin\phi\right)\right)\cos\phi\end{aligned} \tag{A.1}$$

During most of the vehicle maneuvering, the vehicle roll motion (ϕ) is small, the above equations can be written as:

$$\begin{aligned}\ddot{\phi} &= \frac{M_x}{I_x} \\ \ddot{\varepsilon} &= \frac{M_z}{I_z}\end{aligned} \tag{A.2}$$

Therefore, the integrated yaw-roll model can be broken into two sub-models: roll model and yaw model. The angular momentum along e_x^B (M_x) consists of lateral force and vertical force while the angular momentum along e_y^B (M_y) consists of longitudinal force and lateral force. Therefore the lateral force is presented in both roll dynamics as well as yaw dynamics.

B. Parameters of the Full-Car Model

In this appendix, the vehicle parameters utilized in simulations are mainly taken the Feng's dissertation [7] and Hingwe's dissertation [13] as reference. Furthermore, vehicle parameters, shown in the following section, consist of three parts: vehicle inertial and geometric parameters, suspension coefficients, and tire geometric and experiential parameters.

B.1 Vehicle Inertial and Geometric Parameters

Vehicle parameters	Symbol	Value	Unit
Total mass of the vehicle	$m_{vehicle}$	1740	kg
Sprung mass of the vehicle	m_s	1600	kg
Front unsprung mass of the vehicle	$m_{u1,2}$	40	kg
Rear unsprung mass of the vehicle	$m_{u3,4}$	30	kg
Roll moment of inertia	I_x	420	$kg \cdot m^2$
Pitch moment of inertia	I_y	2594	$kg \cdot m^2$
Yaw moment of inertia	I_z	3214	$kg \cdot m^2$
Front tread width	sb_1	1.45	m
Rear tread width	sb_2	1.45	m
Distance from the CG to the front axis	l_1	1.05	m
Distance from the CG to the rear axis	l_2	1.4	m
Height of the vehicle shell	h	0.6	m
Distance from the CG to the road	Z	0.7	m
Gravitational constant	g	9.81	m/s^2

Table B.1 The inertial and geometric parameters of the full-car model

B.2 Suspension Coefficients

The equations of the suspension, shown in section 2.3.2, contain the nonlinear stiffness coefficient and the damper coefficient. Then, suspension coefficients are listed in table B.2.

B.3 Tire Geometric and Experiential Parameters

Tire geometric parameters, shown in section 2.3, are listed in table B.3.

Tire experiential parameters of the nonlinear tire model, shown in section 2.3.3, are verified by Feng [7]. Furthermore, these tire experiential parameters, which consist of two parts: parameters in the longitudinal direction and parameters in the lateral direction, are listed in table B.4 and table B.5, respectively. Additionally, the more information for this nonlinear tire model is shown in Pacejka [15] [16].

Suspension coefficients	Symbol	Value	Unit
Spring stiffness coefficient	C_1	34000	N/m
Spring stiffness coefficient	C_2	300	N/m
Spring stiffness coefficient	C_3	0.21	m
Damper damping coefficient	D_{damper}	1200	$N \cdot s/m$

Table B.2 Coefficients of the nonlinear suspension model

Tire geometric parameters	Symbol	Value	Unit
Real radius of the tre	r	0.3	m
Moment of inertia of the tire	I_{wheel}	2.03	$kg \cdot m^2$
Vertical stiffness coefficient	$K_{vertical}$	150000	N/m
Front roll steer coefficient	$\kappa_{1,2}$	0.01	
Rear roll steer coefficient	$\kappa_{3,4}$	0.03	
Camber trust coefficient	γ	1000	N/rad

Table B.3 Tire geometric parameters

Nonlinear tire model parameters	Symbol	Value(tracking)	Value (braking)
Tire coefficient, stiffness factor	B_x	$22+\frac{F_z-1940}{645}$	$22+\frac{F_z-1940}{430}$
Tire coefficient, shape factor	C_x	$1.35-\frac{F_z-1940}{16125}$	$1.35-\frac{F_z-1940}{16125}$
Tire coefficient, peak value	D_x	$2000+\frac{F_z-1940}{0.956}$	$1750+\frac{F_z-1940}{0.956}$
Tire coefficient, curvature factor	E_x	-3.6	0.1

Table B.4 Nonlinear tire stiffness coefficients in the longitudinal direction

Nonlinear tire model parameters	Symbol	Value
Tire coefficient, stiffness factor	B_y	$2.2+\frac{5200-F_z}{4000}$
Tire coefficient, shape factor	C_y	$1.26+\frac{5200-F_z}{32750}$
Tire coefficient, peak value	D_y	$-0.0003F_z^{\ 2}+1.8096F_z-22.73$
Tire coefficient, curvature factor	E_y	-1.6

Table B.5 Nonlinear tire stiffness coefficients in the lateral direction